

1 **Aerosol Optical Properties over an Urban Site in Central China**
2 **Determined Using Ground-based Sun Photometer Measurements**

3
4 **Chao Liu^{1,2}, Leiku Yang^{1*}, Huizheng Che^{2†}, Xiangao Xia^{3,4}, Hujia Zhao^{2,5},**
5 **Hong Wang², Ke Gui², Yu Zheng^{2,6}, Tianze Sun², Xiaopan Li², Zhizhong**
6 **Sheng², Han Wang¹, Xiaofeng Lu¹, Xiaoye Zhang²**

7
8 ¹ *School of Surveying and Land Information Engineering, Henan Polytechnic University, Jiaozuo*
9 *454000, Henan, China*

10 ² *State Key Laboratory of Severe Weather (LASW), Institute of Atmospheric Composition,*
11 *Chinese Academy of Meteorological Sciences, Beijing 100081, China*

12 ³ *Laboratory for Middle Atmosphere and Global Environment Observation (LAGEO), Institute of*
13 *Atmospheric Physics, Chinese Academy of Sciences, Beijing 100029, China*

14 ⁴ *School of Geoscience University of Chinese Academy of Science, Beijing 100049, China*

15 ⁵ *Institute of Atmospheric Environment, China Meteorological Administration, Shenyang 110016,*
16 *China*

17 ⁶ *Collaborative Innovation Center on Forecast and Evaluation of Meteorological Disasters,*
18 *Nanjing University of Information Science & Technology, Nanjing 210044, China*

20 **Abstract**

21
22 Sun photometer measurements at urban Jiaozuo in Central China from July 2016 to February
23 2018 were used to investigate the aerosol optical and microphysical properties, including the
24 climatological variation of aerosol properties, aerosol classification and aerosol properties under
25 haze and dust events. The annual mean aerosol optical depth at 440 nm ($AOD_{440\text{ nm}}$) and the
26 Ångström exponent ($AE_{440-870\text{ nm}}$) were 0.84 ± 0.55 and 1.12 ± 0.17 , respectively. The highest
27 AOD being in summer may be associated with the hygroscopic growth of aerosols under
28 enhanced relative humidity. Accordingly, high volume of fine-mode particles was observed in
29 summer. In addition, the carbonaceous aerosols from biomass burning increased the volume of
30 fine particles in June and September. Whereas the coarse-mode particles (mainly dust) dominated

*Corresponding author.

Tel: 86-0391-3987661; Fax: 86-0391-3987663

E-mail address: yanglk@hpu.edu.cn

†Corresponding author.

Tel: 86-10-58993116; Fax: 86-10-62176414

E-mail address: chehz@cma.gov.cn

31 during spring, especially in May with a maximum volume of $0.16 \mu\text{m}^3 \mu\text{m}^{-2}$. The seasonal mean
32 single scattering albedo at 440 nm ($\text{SSA}_{440 \text{ nm}}$) was lower in spring (0.87 ± 0.05) and higher in
33 summer (0.95 ± 0.04). On the contrary, absorption aerosol optical depth at 440 nm ($\text{AAOD}_{440 \text{ nm}}$)
34 was higher during spring (0.079 ± 0.019) and lower during summer (0.045 ± 0.021). The
35 increased absorptivity of aerosols in spring and strong scattering ability in summer may be
36 associated with aerosol particles from different sources. The predominant aerosol type was
37 absorbing aerosols (fine and mixed) according to the classification technique using fine mode
38 fraction (FMF), SSA and AE. This urban site was not only influenced by anthropogenic aerosols
39 from local emissions and the surrounding regions but also affected by dust from northwestern
40 China. The mean AOD and AE were 1.66 and 1.38 on haze days, while slightly low AOD of 0.95
41 and extremely low AE of 0.18 on dust days. This study provides a comprehensive understanding
42 of aerosol properties in this area, and the results will help to optimize the satellite aerosol
43 inversion algorithm and promote regional climate change research.

44

45 **Keywords:** Aerosol optical properties; Aerosol classification; Sun photometer measurements;
46 Jiaozuo.

47

48 **INTRODUCTION**

49

50 Aerosol particles are an important component of the earth–atmosphere system, directly
51 influencing its radiative energy balance by absorbing and scattering solar radiation (Kaufman et
52 al., 1997), and indirectly altering the microphysical properties of cloud by acting as cloud
53 condensation nuclei (Twomey et al., 1984). In addition, atmospheric aerosol, as a major pollutant
54 in the atmosphere, can cause various atmospheric environmental problems, such as the
55 degradation of air quality (Seneviratne et al., 2017) and visibility (Che et al., 2007), ultimately
56 threatening human health (Pope and Dockery, 2006; Kumar et al., 2015). Therefore, long term
57 measurements of aerosol optical properties need to be conducted for further exploring the effects
58 of aerosols on climate change and environmental pollution.

59 Due to the high variability in the spatial and temporal distribution of the optical and
60 microphysical properties of aerosol particles (Liu et al., 2009; Ma et al., 2011), their impact on
61 Earth's climate is highly uncertain (Schwartz and Andreae, 1996; Hansen et al., 2000). Therefore,
62 a large number of aerosol in-situ measurements of the optical and microphysical properties is
63 imperative. Satellite remote sensing and ground-based observation are two effective methods for
64 measuring aerosol, each with their own strengths and weaknesses. Satellite remote sensing can
65 detect continuous distributions of aerosol features [e.g., aerosol optical depth (AOD)] (Zhang et
66 al., 2018; He et al., 2018; Qin et al., 2018) and quickly obtain global-scale aerosol information on
67 them regardless of the limits imposed by conditions on the ground; however, some other aerosol
68 optical properties, e.g., absorption aerosol optical depth (AAOD) and absorption Ångström
69 exponent (AAE), are harder to retrieve via this route. Ground-based observation, meanwhile, is

70 an effective approach for characterizing the optical and microphysical properties of aerosols and
71 can achieve high levels of accuracy (Dubovik and King, 2000). Although ground-based
72 observation can only reflect aerosol information within a certain range around a site, a number of
73 global or regional aerosol observation networks have been established worldwide. For example,
74 AERONET (Holben et al., 1998), PHOTONS (Goloub et al., 2008), SKYNET (Nakajima et al.,
75 2003), AEROCAN (Bokoye et al., 2001), and CARSNET (Che et al., 2009; Che et al., 2015a).

76 In recent decades, China has experienced a period of rapid economic development that has
77 attracted worldwide attention. Accompanied by the rapid increase in the level of industrialization
78 and urbanization, many cities have encountered severe air pollution with considerable
79 contributions from atmospheric particulate matter (PM) (Chan and Yao, 2008). These aerosol
80 particles are mainly derived from natural sources and anthropogenic emissions. Aerosol particles
81 are not usually homogeneous in most Chinese cities; rather, they are made up of a mixture of
82 absorbing and non-absorbing particles. Absorbing aerosol particles include carbonaceous aerosols
83 produced by coal combustion and biomass burning, as well as iron oxides in mineral dust (Yang
84 et al., 2009). Non-absorbing aerosols comprise not only sulfate and nitrate emitted by the burning
85 of fossil fuel and present in vehicle exhaust, but also ammonium-salt and sea-salt. A great
86 number of studies on aerosol optical properties have been conducted in China, together
87 contributing immensely to our understanding of urban air pollution (Che et al., 2015b; Li et al.,
88 2016; Zhao et al., 2018). For example, Li et al. (2017) studied the optical and microphysical
89 properties of aerosols in summer in North China; aerosol optical properties and direct radiative
90 forcing in Northeast China were analysed by Che et al. (2015c); and Wang et al. (2011) reported

91 seasonal changes in aerosol optical characteristics in different regions of China. However, most
92 studies of this type have concentrated mainly on the Yangtze River Delta (YRD) region (Cheng
93 et al., 2015; Qi et al., 2016; Che et al., 2018), the North China Plain (Che et al., 2014; Zhu et al.,
94 2014; Zheng et al., 2017), Northeast China (Wang et al., 2010; Zhao et al., 2013; Che et al.,
95 2015c), and some other heavily polluted areas (Wang et al., 2015a; Li et al., 2017; Liu et al.,
96 2017). Only a few studies have focused on the aerosol optical properties in central China, due to
97 the limited availability of aerosol observations in this region. Among those few studies, Wang et
98 al. (2015a, 2015b) and Zhang et al. (2017a) used ground-based observation data to study the
99 aerosol optical properties in the areas of Wuhan and Songshan mountain; yet, to the best of our
100 knowledge, due to short of ground site or observation, no attempt has been made to investigate
101 the aerosol optical and microphysical properties in an urban region in Henan Province which has
102 suffered from serious air pollution. Crucially, Henan Province is located in the Beijing–Tianjin–
103 Hebei atmospheric transmission channel, meaning its aforementioned serious air pollution may
104 have measurable effects on the air quality over the Beijing–Tianjin–Hebei region, which,
105 socioeconomically, is a highly important part of China. Therefore, it is imperative to study the
106 aerosol optical properties in this area for improving our understanding of local air pollution and
107 regional aerosol-climate interactions.

108 The purpose of the present reported work was to investigate the aerosol optical properties in
109 Jiaozuo using one and a half years (July 2016 to February 2018) of ground-based sun photometer
110 data. Specifically, monthly and seasonal variations of AOD, AAE, AAOD, Ångström exponent
111 (AE), single scattering albedo (SSA), and volume size distribution were analysed. Additionally,

112 two typical pollution processes (namely, haze and dust) were selected to analyse the aerosol
113 optical properties and identify the sources of aerosol. The results of this study reflect the
114 characteristics of aerosol optical properties in Henan, and to a certain extent even in other urban
115 areas of central China, and may assist in improving the aerosol model over China, optimizing
116 satellite aerosol inversion algorithms and advancing regional climate change research.

117

118 SITE, DATA AND METHODS

119

120 *Site and Instruments*

121 Fig. 1 shows the geographic location of the Jiaozuo-HPU site, which is the only urban site in
122 Henan Province for measuring aerosol optical properties. The site is on the campus of Henan
123 Polytechnic University (HPU) in the city of Jiaozuo, Henan Province, China, where a CE-318 sun
124 photometer (Cimel Electronique, Paris, France) was installed on the roof of the School of
125 Surveying and Land Information Engineering building (35.3°N , 113.3°E , 113 m) in July 2016.
126 Jiaozuo is an industrial city located in northwestern Henan Province, with the Taihang
127 Mountains to the north and the Yellow River to the south, about 60 km from Zhengzhou (the
128 capital of Henan Province). The climate type in Jiaozuo is northern temperate monsoon, typified
129 by abundant rainfall and high temperatures in summer.

130 The type of sun photometer at Jiaozuo-HPU is CE318N-EDPS9 which is termed as polarized
131 version. It can measure direct solar radiation for each 15 minutes in nine bands (1640, 1020, 870,
132 670, 500, 440, 380, 340, and 936 nm) with a 1.2° full field-of-view (Holben et al., 1998).
133 Measurements in the first eight bands can be used to retrieve the spectral AOD, while total
134 precipitable water vapor can be obtained by the strong water vapor absorption band at 936 nm

135 (Holben et al., 1998; Che et al., 2009). The level 1.5 AOD data [cloud-screened AOD, according
136 to Smirnov et al. (2000)] from July 2016 to February 2018 were calculated in the ASTPwin
137 software (Cimel Ltd. Co.). To achieve more reliable results, only AODs observed more than 10
138 times a day and on 10 days or more in a month were used to calculate the daily and monthly
139 AOD, respectively (Che et al., 2009; Zhao et al., 2013) (Table 1). The AE (α) was derived from
140 the AOD between 440 and 870 nm by Eq. (1) as follows:

$$141 \quad \alpha = -\frac{\ln(\tau_1/\tau_2)}{\ln(\lambda_1/\lambda_2)} \quad (1)$$

142 where τ_1, τ_2 are AOD at bands of λ_1 and λ_2 respectively.

143 In addition, the aerosol microphysical properties and other optical properties, such as SSA,
144 AAOD, AAE, and volume size distribution, were retrieved from the almucantar sky radiance
145 observations at 440, 670, 870 and 1020 nm, in conjunction with the measured AOD (Dubovik
146 and King, 2000; Dubovik et al., 2002; Che et al., 2009; Zhao et al., 2013). Among them, AAOD
147 and AAE were calculated by Eqs. (2) and (3) (Russell et al., 2010; Giles et al., 2012).

$$148 \quad \text{AAOD}(\lambda) = \text{AOD}(\lambda) \times (1 - \text{SSA}(\lambda)) \quad (2)$$

$$149 \quad \text{AAE} = -d \ln[\text{AAOD}(\lambda)]/d \ln(\lambda) \quad (3)$$

150
151 The uncertainty of AOD is approximately 0.01-0.02 (Eck et al., 1999). The SSA with error of
152 about 0.03 can be retrieved only for $\text{AOD}_{440\text{ nm}} \geq 0.40$ for solar zenith angles $> 50^\circ$, to avoid
153 the larger error from the limited information content under lower AODs (Dubovik et al., 2002;
154 Che et al., 2015c).

155

156 ***Data and Analytical Methods***

157 In this work, in addition to the CE-318 sun photometer data, meteorological data (relative
158 humidity and wind speed) from the China Meteorological Administration and hourly

159 observations of PM concentrations from the China National Environmental Monitoring Centre
160 (<http://www.cnemc.cn/>) were used to investigate the variation in aerosol optical properties during
161 the two pollution processes of haze and dust. We also used ERA-Interim data
162 (<http://apps.ecmwf.int/datasets>) downloaded from the European Centre for Medium-Range
163 Weather Forecasts (ECMWF) to analyse the wind field variation at different pressure levels
164 during these pollution processes. Moderate Resolution Imaging Spectroradiometer (MODIS) true
165 color images, with a spatial resolution of 1×1 km, were used, to identify dust storms, fog and
166 haze, and cirrus cloud. During the dust episode, the Cloud-Aerosol Lidar and Infrared Pathfinder
167 Satellite Observation (CALIPSO) data was also used to provide vertical profiles of aerosol and
168 cloud layers and aerosol subtypes (Omar et al., 2009). In this work, we mainly analyzed the
169 nighttime CALIPSO V3.40 data and the daytime data was only as a reference due to being
170 influenced by the noise of solar radiation.

171 The 72-h backward trajectories arriving at Jiaozuo-HPU at multiple altitudes were calculated
172 using software called TrajStat (Ngan et al., 2015). We also used Potential Source Contribution
173 Function (PSCF) analysis to further determine the probable source locations of the pollution (Xin,
174 2016). The Concentration Weighted Trajectory (CWT) method was also applied in this regard,
175 because of its advantages in separating strong and weak sources, which is something PSCF is
176 unable to do. To reduce the level of uncertainty in the values obtained, a weighting function was
177 applied for PSCF and CWT (WPSCF and WCWT, respectively).

178

179 **RESULTS AND DISCUSSION**

180

181 ***Particle Radius and Volume Size Distributions***

182 The effective radii of aerosol particles in the Jiaozuo area are listed in Table 1. The monthly
183 effective radii of the total particles varied between 0.30 and 0.45 μm , and the annual mean
184 effective radii of fine-mode and coarse-mode particles were 0.17 and 2.12 μm , respectively.
185 Remarkably, the fine-mode aerosol effective radii in summer (June–August) (0.19–0.22 μm)
186 were larger than those in spring (March–May) (0.14–0.15 μm). This result may be attributable to
187 aerosol hygroscopicity in summer (Che et al., 2018). The monthly mean aerosol volume and size
188 distribution are shown in Fig. 2. Clearly, the size distribution in Jiaozuo has a typical bimodal
189 distribution (Fig. 2(a)). There were slight differences in the peak radii for fine-mode and
190 coarse-mode particles in different months, in which the fine-mode particle radii were mainly
191 concentrated within 0.15–0.35 μm and the coarse-mode particle radii within 1.9–3.5 μm .

192 From Fig. 2(b), the volume of coarse-mode aerosol particles was obviously higher than that of
193 fine-mode particles in spring. In April and May, coarse-mode particles accounted for the highest
194 proportion, exceeding 65%. The percentage was 66.73% in May, with a volume of
195 0.16 $\mu\text{m}^3\mu\text{m}^{-2}$, which was twice as much as the fine mode particles. It is also evident, from the
196 size distribution (Fig. 2(a)), that the coarse mode particles were dominant in April and May, with
197 peak radii of 2.4 and 1.8 μm , respectively. This may be due to the area being located in the
198 middle and lower reaches of the Yellow River, where the soil is loose and strong winds in spring
199 cause localized blowing-sand weather to enhance the concentration of coarse particles in the
200 atmosphere. In addition, long-distance dust transportation from northwestern China in spring may
201 lead to elevated coarse-particle concentrations (Che et al., 2011). Indeed, Sun et al. (2018)

202 highlighted that Henan Province (Jiaozuo) is located on the pathway of dust particles being
203 transported from northwestern China to the YRD region.

204 In summer, the volume of coarse particles decreased significantly compared with spring; the
205 percentage in July and August was only about 30%. This may be attributable to the removal of
206 coarse particles by heavy precipitation. The dominance of the fine mode particles in summer is
207 also apparent in the size distribution and the peak radii moving toward the shortwave infrared
208 wavelengths with the increase in precipitation from June to August (Fig. 3(c)); specifically, the
209 radius increased from 0.2 to $0.35\mu\text{m}$. The reason is that the size of hygroscopic aerosol,
210 containing sulfate, nitrate and ammonium, is strongly influenced by high relative humidity (Shen
211 et al., 2015; Huang et al., 2016). Furthermore, similar results have been observed in different
212 areas of China, such as the North China Plain (Zhu et al., 2014), Northeast China (Che et al.,
213 2015c), and the YRD region (Che et al., 2018). However, there are slight differences in some of
214 the details. For example, a high volume of fine-mode particles was reported in June and
215 September in the YRD region, owing to the mei-yu floods and autumn-rain, but a relatively low
216 volume in July and August thanks to subtropical anticyclonic circulation (Che et al., 2018). The
217 strong precipitation that occurred in July and August in Jiaozuo and the high volume for the fine
218 mode particles in June and September may have been due to increased concentrations of black
219 carbon aerosol caused by the burning of wheat and corn crops. The volume of fine-mode particles
220 reached 0.16 , 0.18 , 0.17 and $0.14 \mu\text{m}^3\mu\text{m}^{-2}$ in June to September, respectively. It should also be
221 noted that Eck et al. (2012) reported that a large size range of fine-mode aerosol particles may be
222 formed by cloud processing.

223

224 ***Aerosol Optical Depth, Ångström Exponent and Water Vapor Content***

225 The annual mean AOD at 440 nm in Jiaozuo was 0.84 (0.73 at 500 nm), with a standard
226 deviation of ± 0.55 , which suggests high aerosol loading. The AOD in Jiaozuo was higher than
227 that reported for Longfengshan in northeastern China (0.35) (Wang et al., 2010), Xinglong in
228 northern China (0.28) (Zhu et al., 2014), and Songshan mountain in central China (0.60 at 500nm)
229 (Wang et al., 2015b), the latter of which is regarded as the regional background site in Henan
230 Province, 90 km south of Jiaozuo-HPU. Additionally, it was also higher than in several
231 metropolises, such as Beijing (0.76) (Che et al., 2015a), Shanghai (0.70) (He et al., 2012a),
232 Hangzhou (0.76) (Che et al., 2018), and Shenyang (0.75) (Zhao et al., 2015). The annual average
233 AE_{440–870 nm} was 1.12 ± 0.17 , suggesting that the main particles in the Jiaozuo area were
234 fine-mode particles.

235 The temporal variations of monthly average AOD_{440 nm}, AE_{440–870 nm}, and water vapor content
236 (WVC) are shown in Fig. 3. As shown in Fig. 3(a), the monthly variation of AOD was significant.
237 The maximum value of AOD was in July, at 1.11 ± 0.59 . The AOD in June, August and
238 September was also relatively high, at 0.98 ± 0.42 , 0.96 ± 0.52 and 1.07 ± 0.72 , respectively.
239 The minimum value of AOD was 0.57 ± 0.41 , in April. The monthly average WVC showed an
240 almost parabolic variation similar to Yangtze River Basin reported by He et al (2017), with high
241 values in June to September and the maximum value (4.71 cm) in July and August (Fig. 3(c)) due
242 to more precipitation. The high AOD values may have been related to the high WVC in these
243 months. As Eck et al. (2005) pointed out, a high WVC in the atmosphere in summer is conducive
244 to the hygroscopic growth of fine particles. Therefore, the hygroscopic effect of fine particles

may have caused high levels of extinction in June to September. Besides, the high AOD in June and September may also have been affected by the burning of crop straw. From Fig. 3(b), the monthly mean AE values were all greater than 0.8, indicating the Jiaozuo area was dominated by fine-mode aerosol during this period. The maximum monthly AE occurred in June (1.37 ± 0.15) and the minimum in April (0.81 ± 0.37), which is consistent with the analysis of aerosol microphysical characteristics mentioned above.

Additionally, there were clear seasonal variations of AOD and AE. The mean values of AOD_{440nm} in four seasons were 0.69 ± 0.41 , 1.02 ± 0.53 , 0.88 ± 0.54 and 0.72 ± 0.61 , respectively. The maximum AOD occurring in summer was likely related to the combined effect of several factors. Firstly, high relative humidity in summer can cause an increase in AOD (Deng et al., 2012). Secondly, the combustion of straw will produce additional aerosol particles. And thirdly, secondary organic aerosol particles can be generated by photochemical reactions under high temperatures in summer (Kroll and Seinfeld, 2008). Compared with autumn (September–November), the AOD in winter (December–February) was lower, possibly associated with governmental efforts to treat air pollution at that time of year. The seasonal average values of AE were 0.92 ± 0.35 , 1.27 ± 0.22 , 1.09 ± 0.25 and 0.98 ± 0.32 , respectively. The AE in spring was lower than in the other seasons, indicating there were more coarse-mode particles in the atmosphere during that season. In summer, abundant precipitation can eliminate coarse-mode particles via wet deposition, meaning the fine mode particles begin to dominate. There was a lower AE in winter compared with the background site at Songshan mountain (1.23). This may be explained by higher levels of fugitive dust in the city (Che et al., 2014).

267 ***Single Scattering Albedo***

268 The SSA is an important optical parameter that characterizes the scattering ability of aerosol,
269 which is the proportion of scattering AOD to total AOD. It is mainly determined by the size and
270 composition of aerosol particles (Dubovik et al., 2002). As shown in Fig. 4, there were distinct
271 month-to-month variations of SSA at different wavelengths (440, 670, 870 and 1020 nm). From
272 February to May, the SSA presents a decreasing trend, reaching a minimum in May, with values
273 of 0.86, 0.87, 0.85 and 0.84 in the four bands, respectively. This tendency reveals the increasing
274 absorptivity of aerosol particles. The SSA increased sharply from May to August and then
275 declined. The seasonal mean values for SSA at 440 nm were 0.87 ± 0.05 , 0.95 ± 0.04 , 0.92 ± 0.05
276 and 0.90 ± 0.04 for spring, summer, autumn and winter, respectively. The minimal SSA in spring,
277 especially in May, implies light-absorbing dust particles in the atmosphere. The maximum SSA
278 in summer can be attributed to hygroscopic growth under high relative humidity, wherein the size
279 of aerosol particles can modify the spectral properties of the SSA, resulting in an increase in its
280 scattering ability (Xia et al., 2007). Meanwhile, the larger difference between the four
281 wavelengths may imply that hygroscopic aerosol particles are more sensitive to wavelength
282 variation. Compared with summer, a slight decrease in autumn was observed, which can be
283 explained by light-absorbing carbonaceous aerosols from biomass burning (Arola et al., 2011).
284 Thereafter, in winter, the greater concentrations of black carbon aerosol particles in the
285 atmosphere generated by domestic heating emissions may be responsible for the relatively lower
286 SSA values in that season. An interesting phenomenon is that the SSAs at 670 nm, 870 nm and
287 1020 nm differed little between autumn and winter, which might be indicative of the SSA being
288 insensitive to wavelength variation within 670–1020 nm because of the presence of carbonaceous

289 aerosols.

290

291 ***Absorption Aerosol Optical Depth and Absorption Ångström Exponent***

292 The AAOD represents the extent of the absorptive extinction of aerosol particles. Fig. 5(a)
293 plots the monthly variation in AAOD at 440 nm. It shows that the maximum value (0.084 ± 0.018)
294 of the monthly mean was reached in May and the minimum (0.038 ± 0.021) in August. The
295 seasonal averages were 0.079 ± 0.019 , 0.045 ± 0.021 , 0.060 ± 0.029 and 0.066 ± 0.036 for spring,
296 summer, autumn and winter, respectively. A high AAOD value generally reflects the absorption
297 properties of carbonaceous aerosols and dust aerosols (Torres et al., 2005). The maximum value
298 of AAOD being in spring reflected the strongest absorption ability occurring in that season
299 because of the long-range transportation of absorptive dust particles from surrounding and remote
300 areas of northwest China. It is worth noting that the AAOD reaching its maximum in spring was
301 accompanied by the minimum SSA, followed by a significant drop when entering the summer
302 season. As a result, the AAOD in summer was at a minimum, suggestive of high concentrations
303 of light-scattering particles. Such a pattern in summer may be associated with the wet deposition
304 of dust particles in the rainy season. Besides, another reasonable explanation for low AAOD is
305 increasing concentrations of secondary aerosols, such as nitrates and sulfates, from different
306 sources (e.g., industrial emissions, photochemical reactions, vehicle exhaust). After summer, the
307 occurrence of black carbon aerosol particles generated by straw combustion in early autumn, as
308 well as the rise in domestic heating later that season, were likely responsible for the increased
309 AAOD in September and November, respectively. As for winter, the AAOD was higher than the
310 values (< 0.05) previously observed in Hangzhou (Che et al., 2018) and Hefei (Liu et al., 2017),

311 but lower than that (0.1) in Shenyang (Zhao et al., 2015). The use of coal for heating purposes
312 produces substantial amounts of absorbing black carbon aerosols in the Jiaozuo area. The same is
313 true of Shenyang; plus, more absorbing particles generated by heavy industry in Shenyang and its
314 surrounding areas contribute there to its high AAOD values. Relatively lower values appear in
315 winter in southern China (e.g., in Hangzhou and Hefei), owing to comparatively low emissions of
316 absorptive particles from domestic heating.

317 The types of absorbing aerosol particles (e.g., black carbon, organic matter, and dust) can be
318 distinguished based on the AAE (Giles et al., 2012). Fig. 5(b) shows the monthly variations of
319 AAE. From April to August, the monthly mean AAE was generally lower than 1. The occurrence
320 of black carbon coated with absorbing or non-absorbing materials has been cited as a possible
321 cause of the AAE being far lower than 1 (Bergstrom et al., 2007; Gyawali et al., 2009). However,
322 it might also be related to measurement uncertainties and/or errors in retrieving the SSA
323 (Dubovik and King, 2000). Thus, more observations are needed in the future to confirm these
324 apparently low AAE values. The average AAE was relatively high (> 1) in the colder months of
325 September to March. Indeed, from the perspective of seasonal variation, the AAE was
326 significantly higher in autumn (1.41 ± 0.26) and winter (1.49 ± 0.36) than in spring ($0.87 \pm$
327 0.25) and summer (0.89 ± 0.30). The AAE values in autumn and winter exceeded 1.10,
328 indicating an obvious increase in organic aerosol concentrations from biomass burning and
329 mineral dust (Lack and Cappa, 2010; Russell et al., 2010). Looking at the year as a whole, the
330 annual mean AAE value was 1.09 ± 0.41 , which is close to 1, possibly indicative of the absorbing
331 aerosols in the Jiaozuo region being primarily composed of black carbon produced by fossil fuel

332 combustion (Bergstrom et al., 2007).

333

334 *Aerosol Type Classification*

335 Aerosols originating from different sources have a diverse range of atmospheric effects
336 (Dubovik et al., 2002; Alam et al., 2016); hence, it is essential in any study like the present one to
337 identify the types of aerosols observed. The mostly commonly used classification technique is
338 correlating the AOD with the AE and then classifying the aerosols into “dust”, “anthropogenic”
339 or “marine”. However, this approach is incapable of sorting aerosols into “absorbing” or
340 “non-absorbing” (Lee et al., 2010; Xia et al., 2016). The absorptivity of aerosol has a substantial
341 effect on the process of direct radiative forcing (IPCC, 2013), which plays a crucial role in
342 quantifying the influence of aerosols on Earth’s climate. It is, however, possibly to distinguish
343 between absorbing and non-absorbing aerosols based on their SSA values (Lee et al., 2010). In
344 addition, the Fine Mode Fraction (FMF), which is defined by $AOD_{\text{fine}(440 \text{ nm})}/AOD_{440 \text{ nm}}$, and
345 the AE, can be used to characterize the dominant size mode of aerosols. In this work, aerosol
346 optical parameters (FMF, SSA and AE) from the Jiaozuo-HPU site were used to classify aerosols
347 into eight types following the method described in Zheng et al. (2017) and Che et al. (2018).
348 Table 2 summarizes the SSA and AE threshold values for the eight types.

349 The aerosol types and their proportions in the Jiaozuo area are illustrated in Figs. 6 and 7,
350 respectively. From Figs. 6(a) and 7(a), we can see that the aerosols were dominated by absorbing
351 fine particles (Type I, II, III) and mixed absorbing particles (Type V), accounting for 36.89% and
352 35.35%, respectively. This indicates that high emissions of absorbing fine-mode aerosols, such as
353 carbonaceous aerosols from agricultural and industrial activities, existed in Jiaozuo. The

354 non-absorbing fine particles (Type IV) accounted for 10.85%, with a value of 0.91 for the FMF,
355 suggesting the presence of some sulfate and nitrate aerosols from the burning of fossil fuel. The
356 proportion of mixed non-absorbing particles (Type VI) was 10.42%, which was slightly lower
357 than the Type IV proportion, and the FMF almost exceeded 0.9. The non-absorbing coarse
358 particles (Type VIII) showed a negligible percentage of total aerosol (0.51%), which might have
359 been associated with the region being far away from the sea. Additionally, a significant seasonal
360 difference in aerosol types is apparent from Figs. 6(b–e) and Figs. 7(b–e). The absorbing coarse
361 particles (mainly dust) (Type VII) accounted for 15.12%, 0%, 4.46% and 6% in the four seasons,
362 respectively, and the FMF varied from 0.44 to 0.52. The highest percentage of dust being in
363 spring was mainly related to the long-range transport activities of that season (Yan et al., 2015);
364 whereas, dust particles were almost eliminated in summer because of heavy rainfall. Owing to the
365 existence of more nitrate and sulfate being produced by high-intensity human activity and/or
366 photochemical reactions under high temperatures (Hennigan et al., 2008), the percentage of Type
367 IV was higher in summer than in other seasons, at 20.87% (FMF: ~0.96). The absorbing
368 fine-mode aerosols (Type I, II, III), as the highest proportion in Jiaozuo, accounted for 34.15%,
369 29.13%, 39.88% and 40.25% in spring, summer, autumn and winter, respectively, and the FMF
370 values of these particles varied from 0.86 to 0.93.

371

372 ***Relationship between AOD and Meteorological Conditions***

373 The accumulation and diffusion of aerosols are both influenced considerably by meteorological
374 factors (Che et al., 2014; Wang et al., 2018). In this next part of our study, we examined the
375 relationship between two such meteorological factors (namely, relative humidity and wind speed)

376 and AOD. Figs. 8(a) and 8(b) show the variation trends of AOD as a function of relative humidity
377 and wind speed, respectively. Clearly, relative humidity and wind speed have opposite effects on
378 aerosol particles. Fig. 8(a) shows that AOD increased with relative humidity, and was only
379 0.30 ± 0.17 in the range of 0–20%. However, the AOD rose to 1.18 ± 0.55 , reaching a
380 maximum, when the relative humidity was greater than 70%. These results indicate that relative
381 humidity has a significant effect on the hygroscopic growth of fine hydrophilic particles (Gui et
382 al., 2016; Zhang et al., 2017b). Besides, Hennigan et al. (2008) reported that secondary aerosol
383 particles, such as NO_3^- and SO_4^{2-} , as well as other secondary organic compounds, form easily in
384 conditions of high relative humidity, which is analogous to the situation in cloud processing. As
385 shown in Fig. 8(b), in contrast, there is negative correlation between AOD and wind speed, and
386 AOD showed a gradual declining trend with higher wind speed. When the wind speed was lower
387 than 1 m/s, the AOD was as high as 0.93 ± 0.57 ; whereas, the AOD dropped to a low level of
388 0.49 ± 0.16 with the wind speed increasing to 5–6 m/s, reflecting the effect of wind on the
389 diffusion of aerosol particles (He et al., 2012b; Gui et al., 2016; Li et al., 2016). The specific
390 impact of the wind direction on pollutants is discussed below in the context of two pollution
391 processes (haze and dust).

392
393 ***Pollution Source Analysis during Dust and Haze Events***

394 To further investigate the variation in aerosol optical properties and pollution sources, two
395 typical pollution outbreak processes (haze and dust) that occurred in Jiaozuo during the study
396 period were selected based on their associated news reports, meteorological data and satellite data.
397 The MODIS true color images during the dust and haze episodes are displayed in Fig. 9.

398 Compared with Figs. 9(a) and 9(g), there is a clear haze coverage over Jiaozuo in Figs. 9(b-f).
399 Figs. 9(i) and 9(j) show the presence of dust. In addition, this dust event can be confirmed by the
400 NASA Earth Observatory (<https://earthobservatory.nasa.gov/NaturalHazards/>).

401 Figs. 10(a) and 10(d) depict the 72-h backward trajectories at multiple heights during the haze
402 and dust cases over Jiaozuo. From Fig. 10(a) it can be seen that the trajectories over haze can be
403 grouped into four clusters. Cluster-4, at an altitude below 500 m, contributes the maximum
404 percentage of 38.89%, which is from the north part of Anhui Province. Cluster-2 accounts for
405 31.48% and originates from southern Shaanxi, passing over northern Shaanxi and southern
406 Shanxi and then to Jiaozuo. The air masses associated with cluster-3 originate from north of
407 Xinjiang, at the highest altitude of 4000 m, accounting for the minimum proportion of 5.56%.
408 Similar to cluster-2, cluster-3 also arrives via southern Shanxi. Cluster-1 originates from the
409 border area between the provinces of Henan, Shandong and Hebei, at an altitude below 500 m,
410 accounting for 24.07%. As shown in Fig. 10(d), the potential source region is mainly located in
411 the area to the northwest of Jiaozuo during dust episodes. The air mass trajectories originate from
412 an altitude above 4000 m and then gradually decline to 2000 m, before eventually travelling
413 across the Taihang Mountains to the receptor site in Jiaozuo. Cluster-1 originates from the Gobi
414 deserts lying on the eastern edge of Xinjiang, accounting for 36.11%, and passes over the Badain
415 Juran Desert and Tengger Desert (Inner Mongolia), northern Ningxia Hui Autonomous Region,
416 northern Shaanxi, southern Shanxi, and then on into Jiaozuo. The air masses associated with
417 cluster-2 have long-range and high-altitude trajectories originating from Russia and travelling
418 over the arid and semi-arid regions of Mongolia (Wang et al., 2006), accounting for 63.89%.

419 When the air masses enter China, they passed over the Ulan Buh Desert, the Mu Us Desert, and
420 southern Shanxi, before reaching Jiaozuo. Hence, cluster-2 has a sizeable effect on PM₁₀
421 concentrations in Jiaozuo.

422 Figs. 10(b) and 10(c) show the results from the WPSCF and WCWT analyses for a haze event
423 that took place from Dec 25 to Dec 31. It is clear that the distributions of WPSCF and WCWT are
424 similar in pattern. In general, the high WPSCF values (> 0.8) are mainly located in Henan
425 Province and surrounding areas, including southern Hebei, western Shandong, northern Anhui,
426 northern Shaanxi, and southern Shanxi, which can be regarded as the most likely source areas.
427 Interestingly, Fig. 10(b) shows the WPSCF values in northern Henan Province to have exceeded
428 0.9, suggesting local emissions contributed greatly to PM_{2.5} concentrations. Meanwhile, it is
429 apparent from Fig. 10(c) that northern Henan, eastern Henan, southern Shaanxi, northern Anhui,
430 southwestern Inner Mongolia, northern Shaanxi, and Southern Shanxi, with rather high WCWT
431 values of around 120 $\mu\text{g}/\text{m}^3$, seemed to be the areas contributing to the deterioration in air
432 quality in Jiaozuo. Indeed, the long and narrow area from southwestern Inner Mongolia to
433 southern Shanxi is an important coal base in China. The mining, utilization and transportation of
434 coal inevitably leads to serious air pollution problems. Southern Hebei and western Shandong,
435 contiguous to Henan Province, also contributed greatly to the PM_{2.5} values of 80–120 $\mu\text{g}/\text{m}^3$.
436 Furthermore, pollutant transport from southern Jiangsu Province (including Shanghai), which is a
437 well-developed region in China with high levels of anthropogenic activity, also increased the
438 accumulation of PM_{2.5} in Jiaozuo, by 90–120 $\mu\text{g}/\text{m}^3$.

439 The distributions of WPSCF and WCWT values under dust conditions showed significant

440 diversity compared with haze days. Unlike the potential sources of haze mentioned above coming
441 from different directions, the region to the northwest of Jiaozuo contributed almost all of the
442 PM₁₀ concentration under dust. The WPSCF value (Fig. 10(e)) in the western part of Inner
443 Mongolia was about 0.5, which Zhang et al. (1998) termed the ‘Northern High Dust Desert’,
444 including the Badain Juran Desert, the Ulan Buh Desert, and the Hobq Desert. The contribution
445 of the ‘Northern High Dust Desert’ to the PM₁₀ loadings in Jiaozuo varied from 100 –
446 200 µg/m³, and was even more than 300 µg/m³ in some areas (Fig. 10(f)). Additionally, the
447 arid and semi-arid areas of western Mongolia contributed to the high PM₁₀ in Jiaozuo by 160 –
448 250 µg/m³. Moreover, what is striking in Figs. 10(e) and 10(f) is that extremely high values of
449 WPSCF (> 0.9) and WCWT (> 300 µg/m³) exist in northern Shaanxi and southern Shanxi
450 provinces, suggesting these areas contributed the most PM₁₀. On the one hand, the air masses
451 associated with cluster-1 and cluster-2 flowed together in Shaanxi and Shanxi; on the other hand,
452 this area was a dust source owing to its location in the eastern part of the Loess Plateau.

453 The atmospheric vertical information including the 532 nm total attenuated backscatter (top),
454 the volume depolarization ratio (middle), and aerosol subtype (bottom) provided by CALIPSO
455 data for the dust event is shown in Fig. 11. Volume depolarization ratio (VDR) can distinguish
456 dust and anthropogenic aerosols (Liu et al., 2008; Tao et al., 2014), and aerosol subtypes include
457 clean marine, dust, polluted and clean continental, polluted dust, and smoke (Omar et al., 2009;
458 Liu et al., 2017). On 3 May and 4 May, the satellite swept across Shaanxi province and Inner
459 Mongolia. The VDR values (> 0.2) indicated that the particles are predominantly non-spherical
460 (dust) on 4 May. The CALIPSO vertical detections showed that dust particles were concentrated

461 at the height of 2-4 km in the middle atmospheric layer. The satellite was across northwestern
462 Henan Province on 5 May, and the height of dust particles has declined according to the aerosol
463 subtype. These airborne dust may follow the air mass in Fig. 10(d) to the Jiaozuo area. On 6 May,
464 the VDR values (> 0.2) were concentrated in upper part of the aerosol layer and dropped to less
465 than 1 km. The aerosol subtype results are also confirmed that the dust particles deposited in
466 Jiaozuo and downstream areas.

467

468 ***Aerosol Optical Properties under Dust and Haze Events***

469 Before analysing the aerosol optical properties during haze and dust events, we investigated the
470 temporal variation of meteorological elements (the wind field) and PM concentrations, both of
471 which contribute to the overall air pollution situation. As Fu et al. (2014) demonstrated, the wind
472 direction can affect the transportation of pollution and determine the spatial distribution of
473 atmospheric pollutants.

474 Figs. 12(a) and 13(a) show the wind field at the surface along with the daily mean $\text{PM}_{2.5}$ and
475 PM_{10} concentrations during the entirety of the haze process that occurred from 25 Dec to 31 Dec.
476 The $\text{PM}_{2.5}$ and PM_{10} concentrations on 25 Dec, the day before the haze “explosion”, were at
477 relatively low levels of $49 \mu\text{g}/\text{m}^3$ and $114 \mu\text{g}/\text{m}^3$, respectively—levels that were lower than
478 China’s national ambient air quality standards (GB3095-2012,
479 http://kjs.mep.gov.cn/hjbhbz/bzwb/dqhjzb/dqhjzlbz/201203/t20120302_224165.htm) ($75 \mu\text{g}/\text{m}^3$ for $\text{PM}_{2.5}$ and $150 \mu\text{g}/\text{m}^3$ for PM_{10}) and therefore suggestive of good air quality in Jiaozuo.
480 This may have been the result of strong southwesterly wind on that day ($> 3 \text{ m/s}$), which was
482 consistent with the direction of the Taihang Mountains being unfavorable for the accumulation

483 of pollutants. The pollutants from eastern Henan and western Shandong were brought to Jiaozuo
484 by easterly wind and southeasterly wind with high speeds ($> 2 \text{ m/s}$) during the development stage
485 of the haze on 26 and 27 Dec. Pollutants gradually accumulated, resulting in an increase in $\text{PM}_{2.5}$
486 and PM_{10} concentrations. This suggests that the haze in the Jiaozuo area was affected not only by
487 local emissions but also by transmission from other areas. Afterwards, the wind speed decreased
488 to below 1 m/s and the $\text{PM}_{2.5}$ concentration increased rapidly to $205 \mu\text{g}/\text{m}^3$ on 28 Dec. On 29
489 Dec, the $\text{PM}_{2.5}$ and PM_{10} concentrations continued to rise, reaching peak values of $245 \mu\text{g}/\text{m}^3$
490 and $340 \mu\text{g}/\text{m}^3$, respectively. Thereafter, the wind direction turned northwesterly with increasing
491 wind speed ($> 4 \text{ m/s}$), creating favorable conditions for the dissipation of pollution. Consequently,
492 the concentration of $\text{PM}_{2.5}$ slumped to $94 \mu\text{g}/\text{m}^3$ on 30 Dec. The decline continued on 31 Dec
493 and the concentrations of $\text{PM}_{2.5}$ and PM_{10} fell to within desirable air quality standards, signalling
494 a complete end to the haze episode.

495 The daily wind fields at 750 hPa (height of 3000 m above ground level) from ERA-Interim
496 (Fig. 12(b)) during a dust event that occurred in May demonstrate how the pollutants from
497 northeastern China were transported to the Jiaozuo area. Northwesterly winds with high speeds
498 ($> 14 \text{ m/s}$) prevailed over northeastern China during this dust event, creating conditions for the
499 transportation of dust. However, strong southeasterly wind was dominant in the Jiaozuo region on
500 3 May, meaning coarse particles did not arrive and there was low PM_{10} ($67 \mu\text{g}/\text{m}^3$) that day (Fig.
501 13(b)). The next day, however, the wind direction at 750 hPa changed from southeasterly to
502 northerly and the wind speed increased to 16 m/s, contributing to the accumulation of PM_{10} mass
503 concentration by $219 \mu\text{g}/\text{m}^3$. The wind speed gradually declined, which was conducive to the

504 formation of stable conditions on 5 March, resulting in the highest PM₁₀ of 440 µg/m³. On 6
505 March, the wind speed increased to 10 m/s, indicating favorable diffusion conditions and leading
506 to a sharp decrease in the concentration of PM₁₀ (116 µg/m³) in Jiaozuo.

507 The aerosol optical properties retrieved from the CE318 sun photometer during haze and dust
508 episodes are exhibited in Fig. 13 (the missing data were mainly due to the accumulation of
509 clouds). Relatively low AOD was observed on 25 Dec, being 0.38, 0.25, 0.21 and 0.19 at 440,
510 670, 870 and 1020 nm, respectively (Fig. 13(a)). On that day, the AE was 0.84, indicating a
511 relatively higher proportion of coarse particles compared with the next few days that the AE
512 varied from 1.34-1.41, and it is also as reflected by the value of 43% for PM_{2.5}/PM₁₀. The AOD
513 showed a sustained increase from 26 Dec to 29 Dec and a maximum value of AOD_{440 nm} (2.54)
514 was observed on 29 Dec. The mean AOD_{440 nm} was 1.66 during this period of haze. Meanwhile,
515 the daily AE was 1.38 and the value of PM_{2.5}/PM₁₀ was larger than 60%, suggesting a large
516 quantity of fine aerosol particles caused this haze. Accordingly, fine-mode particles dominated
517 during the haze “explosion” (27 Dec). The result is analogous to that reported by Zheng et al.
518 (2017). On 30 Dec, the strong northwesterly (> 4m/s) mentioned above in Jiaozuo favored the
519 horizontal diffusion of aerosol particles, and the AOD_{440 nm} decreased to 0.57. On the same day,
520 the AE dropped dramatically to 0.18, suggesting an increase in the concentration of coarse
521 particles. It is clear from Fig. 13(c) that coarse particles were dominant on 30 Dec, with a volume
522 of 0.27 µg/m³ for the coarse mode particles. This may have been related to elevated levels of
523 fugitive dust under the high wind speeds (Che et al., 2014), which might explain why the
524 minimum value of SSA_{440 nm} occurred on 30 Dec. During the haze “explosion” (27 Dec), the

525 larger difference within 670-1020 nm may imply that fine aerosol particles are more sensitive to
526 longer wavelength compared with coarse particles. Of note is that the value of AAOD during this
527 haze was higher than on the clean day (25 Dec and 31 Dec), suggesting a large number of
528 absorptive aerosol particles existed in the atmosphere.

529 The dust originating from the area to the northwest of Jiaozuo caused this dust storm in early
530 May analyzed above. On 3 May, the day before the dust storm, the AE was 1.27 and the AOD at
531 440 nm was 0.85. The AOD in the four bands gradually increased over the next two days,
532 coinciding with the AOD at 440 nm to be 0.90 on 4 May and 0.99 on 5 May, which means that
533 the mean AOD reached 0.95 during the dust event. Correspondingly, the AE declined sharply,
534 reaching extremely low levels of around 0.18 because of increasing concentrations of coarse
535 particles. Furthermore, compared with 3 May, the coarse mode particles were remarkably
536 dominant on 4 May, the peak radius of which was around 1.3 μm . The volume of coarse particles
537 was also twice as large as it was the day before, accompanied by a rise in AAOD and a drop in
538 SSA, to 0.11 and 0.88 respectively, at the wavelength of 440 nm. In short, the absorptive ability
539 of aerosol particles increased on 4 May. The High volumes of coarse particles observed on 6 May
540 might be related to dry deposition of dust particles or more fugitive dust in the atmosphere.

541

542 CONCLUSION

543

544 To the best of our knowledge, this is the first study to have carried out a detailed analysis of the
545 aerosol optical and microphysical properties at Jiaozuo-HPU, an urban site in Henan Province
546 with important implications for the Beijing–Tianjin–Hebei region. Our study was performed from

547 July 2016 to February 2018, during which time we also analyzed cases of two typical pollution
548 processes (dust and haze) to further investigate the aerosol optical properties and pollution
549 sources. The following conclusions can be drawn from our work:

550 The aerosol volume size distributions showed significant monthly and seasonal variations.
551 Coarse-mode aerosol particles dominated in spring, with a maximum concentration of 0.16
552 $\mu\text{m}^3 \mu\text{m}^{-2}$ in May, possibly related to large quantities of mineral dust particles brought by dust
553 storms in that season, as well as localized blowing-sand weather. Low volumes of coarse particles
554 were observed in summer owing to wet removal by abundant rainfall. In contrast, the highest
555 volumes of fine-mode aerosols occurred in summer, and their peak radii moved toward longer
556 wavelengths, from 0.2 μm in June to 0.35 μm in August, which was associated with the
557 hygroscopic growth of fine hydrophilic aerosols under conditions of high relative humidity. In
558 addition, carbonaceous aerosols from biomass burning in June and September increased the
559 volume of fine particles.

560 The monthly mean values of $\text{AOD}_{440 \text{ nm}}$ varied from 0.57 ± 0.41 in April to 1.11 ± 0.59 in
561 July, with an annual mean of 0.84 ± 0.55 , suggesting a high aerosol loading in the Jiaozuo area.
562 The seasonal mean $\text{AOD}_{440 \text{ nm}}$ values were 0.69 ± 0.41 , 1.02 ± 0.53 , 0.88 ± 0.54 and
563 0.72 ± 0.61 for spring, summer, autumn and winter, respectively. The highest AOD being in
564 summer was attributed to the hygroscopic growth of aerosols under enhanced relative humidity,
565 increased agricultural activity (e.g., biomass combustion) and the formation of secondary aerosol
566 particles (e.g., sulfate and nitrate). The annual mean AE was 1.12 ± 0.17 , indicating that fine
567 particles were dominant in Jiaozuo. A lower AE occurred in spring (0.92 ± 0.35) compared with

568 the other seasons, reflecting the existence of more coarse-mode particles in that season. The
569 monthly SSA ($\text{AAOD}_{440 \text{ nm}}$) presented a decreasing (increasing) trend from February to May,
570 which revealed the increasing absorptivity of aerosols, and increased (decreased) sharply from
571 May to August. A distinct seasonal variation in SSA was also observed, with the highest value in
572 summer (0.95 ± 0.04) and the lowest value in spring (0.87 ± 0.05). On the contrary, $\text{AAOD}_{440 \text{ nm}}$
573 was higher in spring (0.079 ± 0.019) and lower in summer (0.045 ± 0.021). The seasonal
574 difference may be due to dust particles in spring, high industrial emissions and hygroscopic
575 growth of fine particles in summer, biomass burning in autumn, and coal combustion for
576 domestic heating in winter. The annual AAE value was 1.09 ± 0.41 , which being close to 1
577 indicated a significant source of absorbing black carbon aerosols from fossil fuel combustion.

578 The aerosols in Jiaozuo were sorted into eight types according to their SSA, FMF and AE
579 values. The absorbing aerosols (fine and mixed) were found to be predominant in the Jiaozuo
580 area, accounting for 36.89% and 35.35% respectively, which we attributed to carbonaceous
581 aerosols from agricultural and industrial activities. An obvious seasonal difference in aerosol
582 types was found. The absorbing coarse particles dominated in spring and accounted for 15.12%,
583 indicating elevated levels of mineral dust particles. The percentage of non-absorbing fine
584 particles was higher in summer than in the other seasons, attributable to the greater abundance of
585 sulfate and nitrate generated by high-intensity human activity and/or photochemical reactions.

586 The enhanced AODs were observed during the two pollution processes of haze and dust. The
587 mean AOD was 1.66 (0.95) on haze (dust) days. A high AE of 1.38 was observed on haze days,
588 suggesting fine-mode aerosol particles were dominant. However, low AE values occurred on dust

589 days because of high concentrations of dust particles being dominant. According to WPSCF and
590 WCWT analysis, pollutants both from surrounding regions and local emissions contributed to this
591 haze episode, while the dust aerosols in this site mainly originated from northwestern China.

592

593 **ACKNOWLEDGMENTS**

594

595 This work is financially supported by grants from National Key R&D Program Pilot Projects
596 of China (2016YFA0601901 & 2016YFC0203306), National Key Project of Basic Research
597 (2014CB441201), National Natural Science Foundation of China (41605112, 41590874,
598 41401403 & 41601392), the CAMS Basis Research Project (2017Z011, 2016Z001 & 2014R17),
599 the Key Technology R&D Program of Henan Province (No. 162102310089), Doctoral foundation
600 of Henan Polytechnic University (No. B2016-14 and B2017-08) and major projects of gaofen
601 satellite (No.30-Y20A010-9007-17/18).

602 **REFERENCES**

603

- 604 Alam, K., Shaheen, K., Blaschke, T., Chishtie, F., Khan, H.U. and Haq, B.S. (2016).
605 Classification of Aerosols in an Urban Environment on the Basis of Optical Measurements.
606 *Aerosol Air Qual. Res.* 16: 2535-2549.
- 607 Arola, A., Schuster, G., Myhre, G., Kazadzis, S., Dey, S. and Tripathi, S.N. (2011). Inferring
608 Absorbing Organic Carbon Content from Aeronet Data. *Atmos. Chem. Phys.* 11: 215-225.
- 609 Bergstrom, R.W., Pilewskie, P., Russell, P.B., Redemann, J., Bond, T.C., Quinn, P.K. and Sierau,

- 610 B. (2007). Spectral Absorption Properties of Atmospheric Aerosols. *Atmos. Chem. Phys.* 7:
611 5937-5943.
- 612 Bokoye, A.I., Royer, A., O'Neill, N.T., Cliche, P., Fedosejevs, G., Teillet, P.M. and Mcarthur,
613 L.J.B. (2001). Characterization of Atmospheric Aerosols across Canada from a Ground-based
614 Sunphotometer Network: Aerocan. *Atmos. Ocean* 39: 429-456.
- 615 Chan, C.K. and Yao, X. (2008). Air Pollution in Megacities in China. *Atmos. Environ.* 42: 1-42.
- 616 Che, H.Z., Zhang, X.Y., Li, Y., Zhou, Z.J. and Qu, J.J. (2007). Horizontal Visibility Trends in
617 China 1981-2005. *Geophys. Res. Lett.* 34: 497-507.
- 618 Che, H.Z., Zhang, X.Y., Chen, H.B., Damiri, B., Goloub, P., Li, Z.Q., Zhang, X.C., Wei, Y., Zhou,
619 H.G., Dong, F., Li, D.P. and Zhou, T.M. (2009). Instrument Calibration and Aerosol Optical
620 Depth Validation of the China Aerosol Remote Sensing Network. *J. Geophys. Res.* 114:
621 D03206.
- 622 Che, H.Z., Zhang, X.Y., Xia, X.A., Goloub, P., Holben, B., Zhao, H.J., Wang, Y.Q., Zhang, X.C.,
623 Wang, H., Blarel, L., Damiri, B., Zhang, R., Deng, X., Ma, Y., Wang, T., Geng, F., Qi, B., Zhu,
624 J., Yu, J., Chen, Q. and Shi, G. (2015a). Ground-based Aerosol Climatology of China: Aerosol
625 Optical Depths from the China Aerosol Remote Sensing Network (Carsnet) 2002-2013. *Atmos.*
626 *Chem. Phys.* 15: 7619-7652.
- 627 Che, H.Z., Zhao, H.J., Xia, X.A., Wu, Y.F., Zhu, J., Ma, Y.J., Wang, Y.F., Wang, H., Wang, Y.Q.,
628 Zhang, X.Y. and Shi, G.Y. (2015b). Fine Mode Aerosol Optical Properties Related to Cloud
629 and Fog Processing over a Cluster of Cities in Northeast China. *Aerosol Air Qual. Res.* 15:
630 2065-2081.

- 631 Che, H.Z., Zhao, H.J., Wu, Y.F., Xia, X.A., Zhu, J., Wang, H., Wang, Y.Q., Sun, J.Y., Yu, J.,
632 Zhang, X.Y. and Shi, G.Y. (2015c). Analyses of Aerosol Optical Properties and Direct
633 Radiative Forcing over Urban and Industrial Regions in Northeast China. *Meteorol. Atmos.*
634 *Phys.* 127: 345-354.
- 635 Che, H.Z., Qi, B., Zhao, H.J., Xia, X.A., Eck, T.F., Goloub, P., Dubovik, O., Estelles, V.,
636 Cuevas-Agulló, E., Blarel, L., Wu, Y.F., Zhu, J., Du, R.G., Wang, Y.Q., Wang, H., Gui, K., Yu,
637 J., Zheng, Y., Sun, T.Z., Chen, Q.L., Shi, G.Y. and Zhang, X.Y. (2018). Aerosol Optical
638 Properties and Direct Radiative Forcing Based on Measurements from the China Aerosol
639 Remote Sensing Network (Carsnet) in Eastern China. *Atmos. Chem. Phys.* 18: 405-425.
- 640 Che, H.Z., Xia, X.A., Zhu, J., Li, Z.Q., Dubovik, O., Holben, B., Goloub, P., Chen, H., Estelles,
641 V., Cuevas-Agulló, E., Blarel, L., Wang, H., Zhao, H.J., Zhang, X.C., Wang, Y.Q., Sun, J.Y.,
642 Tao, R., Zhang, X.Y. and Shi, G.Y. (2014). Column Aerosol Optical Properties and Aerosol
643 Radiative Forcing during a Serious Haze-fog Month over North China Plain in 2013 Based on
644 Ground-based Sunphotometer Measurements. *Atmos. Chem. Phys.* 14: 2125-2138.
- 645 Che, H.Z., Wang, Y.Q. and Sun, J.Y. (2011). Aerosol Optical Properties at Mt. Waliguan
646 Observatory, China. *Atmos. Environ.* 45: 6004-6009.
- 647 Cheng, T.T., Xu, C., Duan, J.Y., Wang, Y.F., Leng, C.P., Tao, J., Che, H.Z., He, Q.S., Wu, Y.F.,
648 Zhang, R.J., Li, X., Chen, J.M., Kong, L.D. and Yu, X.N. (2015). Seasonal Variation and
649 Difference of Aerosol Optical Properties in Columnar and Surface Atmospheres over Shanghai.
650 *Atmos. Environ.* 123: 315-326.
- 651 Deng, X.L., Shi, C.N., Wu, B.W., Chen, Z.H., Nie, S.P., He, D.Y. and Zhang, H. (2012). Analysis

- 652 of Aerosol Characteristics and Their Relationships with Meteorological Parameters over Anhui
653 Province in China. *Atmos. Res.* 109–110: 52-63.
- 654 Dubovik, O. and King, M.D. (2000). A Flexible Inversion Algorithm for Retrieval of Aerosol
655 Optical Properties from Sun and Sky Radiance Measurements. *J. Geophys. Res.* 105:
656 20673-20696.
- 657 Dubovik, O., Holben, B.N., Eck, T.F., Smirnov, A., Kaufman, Y.J., King, M.D., Tanré, D. and
658 Slutsker, I. (2002). Variability of Absorption and Optical Properties of Key Aerosol Types
659 Observed in Worldwide Locations. *J. atmos. sci.* 59: 590-608.
- 660 Eck, T.F., Holben, B.N., Reid, J.S., Dubovik, O., Smirnov, A., O'Neill, N.T., Slutsker, I. and
661 Kinne, S. (1999). Wavelength Dependence of the Optical Depth of Biomass Burning, Urban,
662 and Desert Dust Aerosols. *J. Geophys. Res.* 104: 31333-31349.
- 663 Eck, T.F., Holben, B.N., Reid, J.S., Giles, D.M., Rivas, M.A., Singh, R.P., Tripathi, S.N., Bruegge,
664 C.J., Platnick, S. and Arnold, G.T. (2012). Fog- and Cloud-induced Aerosol Modification
665 Observed by the Aerosol Robotic Network (Aeronet). *J. Geophys. Res.* 117: 107-116.
- 666 Eck, T.F., Holben, B.N., Dubovik, O., Smirnov, A., Goloub, P., Chen, H.B., Chatenet, B., Gomes,
667 L., Zhang, X.Y., Tsay, S.C., Ji, Q., Giles, D. and Slutsker, I. (2005). Columnar Aerosol Optical
668 Properties at Aeronet Sites in Central Eastern Asia and Aerosol Transport to the Tropical
669 Mid-pacific. *J. Geophys. Res. Atmos.* 110: 887-908.
- 670 Fu, G.Q., Xu, W.Y., Yang, R.F., Li, J.B. and Zhao, C.S. (2014). The Distribution and Trends of
671 Fog and Haze in the North China Plain over the Past 30 Years. *Atmos. Chem. Phys.* 14:
672 11949-11958.

- 673 Giles, D.M., Holben, B.N., Eck, T.F., Sinyuk, A., Smirnov, A., Slutsker, I., Dickerson, R.R.,
674 Thompson, A.M. and Schafer, J.S. (2012). An Analysis of Aeronet Aerosol Absorption
675 Properties and Classifications Representative of Aerosol Source Regions. *J. Geophys. Res.* 117:
676 1-16.
- 677 Goloub, P., Li, Z., Dubovik, O., Blarel, L., Podvin, T., Jankowiak, I., Lecoq, R., Deroo, C.,
678 Chatenet, B., Morel, J.P., Cuevas, E. and Ramos, R. (2008). Photons/Aeronet Sunphotometer
679 Network Overview. Description, Activities, Results. *Proc. SPIE* 6936: 69360V.
- 680 Gui, K., Che, H.Z., Chen, Q.L., An, L.C., Zeng, Z.L., Guo, Z.Y., Zheng, Y., Wang, H., Wang, Y.Q.,
681 Yu, J. and Zhang, X.Y. (2016). Aerosol Optical Properties Based on Ground and Satellite
682 Retrievals during a Serious Haze Episode in December 2015 over Beijing. *Atmosphere* 7: 70.
- 683 Gyawali, M., Arnott, W.P., Lewis, K. and Moosmüller, H. (2009). In Situ Aerosol Pptics in Reno,
684 NV, USA during and after the Summer 2008 California Wildfires and the Influence of
685 Absorbing and Non-absorbing Organic Coatings on Spectral Light Absorption. *Atmos. Chem.
686 Phys.* 9: 8007-8015.
- 687 Hansen, J., Sato, M., Ruedy, R., Lacis, A. and Oinas, V. (2000). Global Warming in the
688 Twenty-first Century: An Alternative Scenario. *Proc. Natl. Acad. Sci. USA* 97: 9875-9880.
- 689 He, L.J., Wang, L.C., Lin, A.W., Zhang, M., Bilal, M. and Wei, J. (2018). Performance of the
690 NPP-VIIRS and Aqua-MODIS Aerosol Optical Depth Products over the Yangtze River Basin.
691 *Remote Sens.* 10: 117.
- 692 He, L.J., Wang, L.C., Lin, A.W., Zhang, M., Bilal, M. and Tao, M.H. (2017). Aerosol Optical
693 Properties and Associated Direct Radiative Forcing over the Yangtze River Basin during

- 694 2001-2015. *Remote Sens.* 9: 746.
- 695 He, Q.S., Li, C.C., Geng, F.H., Yang, H.Q., Li, P.R., Li, T.T., Liu, D.W. and Pei, Z. (2012a).
- 696 Aerosol Optical Properties Retrieved from Sun Photometer Measurements over Shanghai,
- 697 China. *J. Geophys. Res. Atmos.* 117: D16204.
- 698 He, Q.S., Li, C.C., Geng, F.H., Lei, Y. and Li, Y.H. (2012b). Study on Long-term Aerosol
- 699 Distribution over the Land of East China Using Modis Data. *Aerosol Air Qual. Res.* 12:
- 700 304-319.
- 701 Hennigan, C.J., Bergin, M.H., Dibb, J.E. and Weber, R.J. (2008). Enhanced Secondary Organic
- 702 Aerosol Formation Due to Water Uptake by Fine Particles. *Geophys. Res. Lett.* 35: L18801.
- 703 Holben, B.N., Eck, T.F., Slutsker, I., Tanré, D., Buis, J.P., Setzer, A., Vermote, E., Reagan, J.A.,
- 704 Kaufman, Y.J., Nakajima, T., Lavenu, F., Jankowia, I. and Smirnov, A. (1998). Aeronet-A
- 705 Federated Instrument Network and Data Archive for Aerosol Characterization. *Remote Sens.*
- 706 *Environ.* 66: 1-16.
- 707 Huang, X., Ding, A.J., Liu, L.X., Liu, Q., Ding, K., Niu, X.R., Nie, W., Xu, Z., Chi, X.G., Wang,
- 708 M.H., Sun, J.N., Guo, W.D. and Fu, C.B. (2016). Effects of Aerosol-radiation Interaction on
- 709 Precipitation during Biomass-burning Season in East China. *Atmos. Chem. Phys.* 16:
- 710 10063-10082.
- 711 IPCC (2013). Climate change 2013: The Scientifical Basis, Cambridge University Press: New
- 712 York, NY, USA.
- 713 Kaufman, Y.J., Tanré, D., Remer, L.A., Vermote, E.F., Chu, A. and Holben, B.N. (1997).
- 714 Operational Remote Sensing of Tropospheric Aerosol over Land from EOS Moderate

- 715 Resolution Imaging Spectroradiometer. *J. Geophys. Res.* 102: 17051-17067.
- 716 Kroll, J.H. and Seinfeld, J.H. (2008). Chemistry of Secondary Organic Aerosol: Formation and
717 Evolution of Low Volatility Organics in the Atmosphere. *Atmos. Environ.* 42: 3593-3624.
- 718 Kumar, M., Singh, R.S. and Banerjee, T. (2015). Associating Airborne Particulates and Human
719 Health: Exploring Possibilities. *Environ. Int.* 84: 201-202.
- 720 Lack, D.A. and Cappa, C.D. (2010). Impact of Brown and Clear Carbon on Light Absorption
721 Enhancement, Single Scatter Albedo and Absorption Wavelength Dependence of Black Carbon.
722 *Atmos. Chem. Phys.* 10: 4207-4220.
- 723 Lee, J., Kim, J., Song, C.H., Kim, S.B., Chun, Y., Sohn, B.J. and Holben, B.N. (2010).
724 Characteristics of Aerosol Types from Aeronet Sunphotometer Measurements. *Atmos. Environ.*
725 44: 3110-3117.
- 726 Liu, B.M., Ma, Y.Y., Gong, W., Zhang, M. and Yang, J. (2018). Study of Continuous Air Pollution
727 in Winter over Wuhan Based on Ground-based and Satellite Observations. *Atmos. Pollut. Res.*
728 9: 156-165.
- 729 Li, J.X., Li, P.R., Yuan, L., Yin, Y., Wang, Z.Z., Li, J., Li, Y.N., Ren, G. and Cai, Z.X. (2017).
730 Physical and Optical Properties of Atmospheric Aerosols in Summer at a Suburban Site in
731 North China. *Aerosol Air Qual. Res.* 17: 1474-1488.
- 732 Li, S.S., Ma, Z.W., Xiong, X.Z., Christiani, D.C., Wang, Z.X. and Liu, Y. (2016). Satellite and
733 Ground Observations of Severe Air Pollution Episodes in the Winter of 2013 in Beijing, China.
734 *Aerosol Air Qual. Res.* 16: 977-989.
- 735 Liu, P.F., Zhao, C.S., Zhang, Q., Deng, Z.Z., Huang, M.Y., Ma, X.C. and Tie, X.X. (2009).

- 736 Aircraft Study of Aerosol Vertical Distributions over Beijing and Their Optical Properties.
- 737 *Tellus* 61: 756–767.
- 738 Liu, Q., Ding, W.D., Xie, L., Zhang, J.Q., Zhu, J., Xia, X.A., Liu, D.Y., Yuan, R.M. and Fu, Y.F.
- 739 (2017). Aerosol Properties over an Urban Site in Central East China Derived from Ground
- 740 Sun-photometer Measurements. *Sci. China Earth Sci.* 60: 297-314.
- 741 Liu, Z.Y., Liu, D., Huang, J.P., Vaughan, M.A., Uno, I., Sugimoto, N., Kittaka, C., Trepte, C.R.,
- 742 Wang, Z.E., Hostetler, C.A. and Winker, D.M. (2008). Airborne Dust Distributions over the
- 743 Tibetan Plateau and Surrounding Areas Derived from the First Year of CALIPSO Lidar
- 744 Observations. *Atmos. Chem. Phys.* 8: 5045-5060.
- 745 Ma, N., Zhao, C.S., Nowak, A., Müller, T., Pfeifer, S., Cheng, Y.F., Deng, Z.Z., Liu, P.F., Xu,
- 746 W.Y., Ran, L., Yan, P., Göbel, T., Hallbauer, E., Mildenberger, K., Henning, S., Yu, J., Chen,
- 747 L.L., Zhou, X.J., Stratmann, F. and Wiedensohler, A. (2011). Aerosol Optical Properties in the
- 748 North China Plain during Hachi Campaign: An in-situ Optical Closure Study. *Atmos. Chem.*
- 749 *Phys.* 11: 5959-5973.
- 750 Nakajima, T., Sekiguchi, M., Takemura, T., Uno, I., Higurashi, A., Kim, D., Sohn, B.J., Oh, S.N.,
- 751 Nakajima, T.Y. and Ohta, S. (2003). Significance of Direct and Indirect Radiative Forcings of
- 752 Aerosols in the East China Sea Region. *J. Geophys. Res.* 108: 2139-2146.
- 753 Ngan, F., Stein, A. and Draxler, R. (2015). Inline Coupling of WRF-HYSPLIT: Model
- 754 Development and Evaluation Using Tracer Experiments. *J. Appl. Meteorol. Clim.* 54:
- 755 1162-1176.
- 756 Omar, A.H., Winker, D.M., Vaughan, M.A., Hu, Y.X., Trepte, C.R., Ferrare, R.A., Lee, K.P. and

- 757 Hostetler, C.A. (2009). The CALIPSO Automated Aerosol Classification and Lidar Ratio
758 Selection Algorithm. *J. Atmos. Ocean. Technol.* 26: 1994-2014.
- 759 Pope, C.A. and Dockery, D.W. (2006). Health Effects of Fine Particulate Air Pollution: Lines
760 That Connect. *J. Air Waste Manage. Assoc.* 56: 709-742.
- 761 Qi, B., Hu, D.Y., Che, H.Z., Du, R.G., Wu, Y.F., Xia, X.A., Zha, B., Liu, J., Niu, Y.W., Wang, H.,
762 Zhang, X.Y. and Shi, G.Y. (2016). Seasonal Variation of Aerosol Optical Properties in an
763 Urban Site of the Yangtze Delta Region of China. *Aerosol Air Qual. Res.* 16: 2884-2896.
- 764 Qin, W.M., Wang, L.C., Lin, A.W., Zhang, M. and Bilal, M. (2018). Improving the Estimation of
765 Daily Aerosol Optical Depth and Aerosol Radiative Effect Using an Optimized Artificial
766 Neural Network. *Remote Sens.* 10: 1022.
- 767 Russell, P.B., Bergstrom, R.W., Shinozuka, Y., Clarke, A.D., DeCarlo, P.F., Jimenez, J.L.,
768 Livingston, J.M., Redemann, J., Dubovik, O. and Strawa, A. (2010). Absorption Angstrom
769 Exponent in Aeronet and Related Data as an Indicator of Aerosol Composition. *Atmos. Chem.
770 Phys.* 10: 1155-1169.
- 771 Seneviratne, S., Handagiripathira, L., Sanjeevani, S., Madusha, D., Waduge, V.A.A., Attanayake,
772 T., Bandara, D. and Hopke, P.K. (2017). Identification of Sources of Fine Particulate Matter
773 in Kandy, Sri Lanka. *Aerosol Air Qual. Res.* 17: 476-484.
- 774 Schwartz, S.E. and Andreae, M.O. (1996). Uncertainty in Climate Change Caused by Aerosols.
775 *Science* 272: 1121-1122.
- 776 Shen, X.J., Sun, J.Y., Zhang, X.Y., Zhang, Y.M., Zhang, L., Che, H.C., Ma, Q.L., Yu, X.M., Yue,
777 Y. and Zhang, Y.W. (2015). Characterization of Submicron Aerosols and Effect on Visibility

- 778 during a Severe Haze-fog Episode in Yangtze River Delta, China. *Atmos. Environ.* 120:
779 307-316.
- 780 Smirnov, A., Holben, B.N., Eck, T.F., Dubovik, O. and Slutsker, I. (2000). Cloud-screening and
781 Quality Control Algorithms for the Aeronet Database. *Remote Sens. Environ.* 73: 337-349.
- 782 Sun, T.Z., Che, H.Z., Qi, B., Wang, Y.Q., Dong, Y.S., Xia, X.A., Wang, H., Gui, K., Zheng, Y.,
783 Zhao, H.J., Ma, Q.I., Du, R.G. and Zhang, X.Y. (2018). Aerosol Optical Characteristics and
784 Their Vertical Distributions under Enhanced Haze Pollution Events: Effect of the Regional
785 Transport of Different Aerosol Types over Eastern China. *Atmos. Chem. Phys.* 18: 2949-2971.
- 786 Tao, M.H., Chen, L.F., Wang, Z.F., Ma, P.F., Tao, J.H. and Jia, S.L. (2014). A Study of Urban
787 Pollution and Haze Clouds over Northern China during the Dusty Season Based on Satellite
788 and Surface Observations. *Atmos. Environ.* 82: 183-192.
- 789 Torres, O., Bhartia, P.K., Sinyuk, A., Welton, E.J. and Holben, B. (2005). Total Ozone Mapping
790 Spectrometer Measurements of Aerosol Absorption from Space: Comparison to Safari 2000
791 Ground-based Observations. *J. Geophys. Res.* 110: D10S18.
- 792 Twomey, S.A., Piepgrass, M. and Wolfe, T.L. (1984). An Assessment of the Impact of Pollution
793 on Global Cloud Albedo. *Tellus* 36B: 356-366.
- 794 Wang, L.C., Gong, W., Xia, X.A., Zhu, J., Li, J. and Zhu, Z.M. (2015a). Long-term Observations
795 of Aerosol Optical Properties at Wuhan, an UrbanSite in Central China. *Atmos. Environ.* 101:
796 94-102.
- 797 Wang, L.C., Gong, W., Singh, R.P., Xia, X.A., Che, H.Z., Zhang, M. and Lin, H. (2015b). Aerosol
798 Optical Properties over Mount Song, a Rural Site in Central China. *Aerosol Air Qual. Res.* 15:

- 799 2051-2064.
- 800 Wang, P., Che, H.Z., Zhang, X.C., Song, Q.I., Wang, Y.Q., Zhang, Z.H., Dai, X. and Yu, D.J.
801 (2010). Aerosol Optical Properties of Regional Background Atmosphere in Northeast China.
802 *Atmos. Environ.* 44: 4404-4412.
- 803 Wang, X., Liu, J., Che, H.Z., Ji, F. and Liu, J.J. (2018). Spatial and Temporal Evolution of Natural
804 and Anthropogenic Dust Events over Northern China. *Sci. Rep.* 8: 2141.
- 805 Wang, Y.Q., Zhang, X.Y. and Arimoto, R. (2006). The Contribution from Distant Dust Sources to
806 the Atmospheric Particulate Matter Loadings at Xian, China during Spring. *Sci. Total Environ.*
807 368: 875-883.
- 808 Wang, Y.S., Xin, J.Y., Li, Z.Q., Wang, S.G., Wang, P.C., Hao, W.M., Nordgren, B.L., Chen, H.B.,
809 Wang, L.L. and Sun, Y. (2011). Seasonal Variations in Aerosol Optical Properties over China. *J.
810 Geophys. Res.* 116: D18209.
- 811 Xia , X.A., Li, Z.Q., Holben , B., Wang, P., Eck, T., Chen, H., Cribb, M. and Zhao, Y. (2007).
812 Aerosol Optical Properties and Radiative Effects in the Yangtze Delta Region of China. *J.
813 Geophys. Res.* 112: D22S12.
- 814 Xia, X.A., Che, H.Z., Zhu, J., Chen, H.B., Cong, Z.Y., Deng, X.J., Fan, X.H., Fu, Y.F., Goloub, P.,
815 Jiang, H., Liu, Q., Mai, B.R., Wang, P.C., Wu, Y.F., Zhang, J.Q., Zhang, R.J. and Zhang, X.Y.
816 (2016). Ground-based Remote Sensing of Aerosol Climatology in China: Aerosol Optical
817 Properties, Direct Radiative Effect and Its Parameterization. *Atmos. Environ.* 124: 243-251.
- 818 Xin, Y. (2016). Identification of Long-range transport Pathways and Potential Sources of PM10 in
819 Tibetan Plateau Uplift Area: Case Study of Xining, China in 2014. *Aerosol Air Qual. Res.* 16:

- 820 1044-1054.
- 821 Yan, Y., Sun, Y.B., Weiss, D., Liang, L.J. and Chen, H.Y. (2015). Polluted Dust Derived from
822 Long-range Transport as a Major End Member of Urban Aerosols and Its Implication of
823 Non-point Pollution in Northern China. *Sci. Total Environ.* 506: 538-545.
- 824 Yang, M., Howell, S.G., Zhuang, J. and Huebert, B.J. (2009). Attribution of Aerosol Light
825 Absorption to Black Carbon, Brown Carbon, and Dust in China – Interpretations of
826 Atmospheric Measurements during East-aire. *Atmos. Chem. Phys.* 9: 2035-2050.
- 827 Zhang, M., Ma, Y.Y., Wang, L.C., Gong, W., Hu, B. and Shi, Y.F. (2018). Spatial-temporal
828 Characteristics of Aerosol Loading over the Yangtze River Basin during 2001-2015. *Int. J.
829 Climatol.* 38: 2138-2152.
- 830 Zhang, M., Wang, L.C., Gong, W., Ma, Y.Y. and Liu, B.M. (2017a). Aerosol Optical Properties
831 and Direct Radiative Effects over Central China. *Remote Sens.* 9: 997.
- 832 Zhang, M., Ma, Y.Y., Gong, W., Wang, L.C., Xia, X.A., Che, H.Z., Hu, B. and Liu, B.M. (2017b).
833 Aerosol Radiative Effect in UV, VIS, NIR, and SW Spectra under Haze and High-humidity
834 Urban Conditions. *Atmos. Environ.* 166: 9-21.
- 835 Zhang, X.Y., Arimoto, R., Zhu, G.H., Chen, T. and Zhang, G.Y. (1998). Concentration,
836 Size-distribution and Deposition of Mineral Aerosol over Chinese Desert Regions. *Tellus* 50:
837 317-330.
- 838 Zhao, H.J., Che, H.Z., Wang, Y.Q., Dong, Y.S., Ma, Y.J., Li, X.X., Hong, Y., Yang, H.B., Liu, Y.C.,
839 Wang, Y.F., Gui, K., Sun, T.Z., Zheng, Y. and Zhang, X.Y. (2018). Aerosol Vertical Distribution
840 and Typical Air Pollution Episodes over Northeastern China during 2016 Analysed by

- 841 Ground-based Lidar. *Aerosol Air Qual. Res.* 18: 918-937.
- 842 Zhao, H.J., Che, H.Z., Zhang, X.Y., Ma, Y.J., Wang, Y.F., Wang, X.X., Liu, C., Hou, B. and Che,
843 H.C. (2013). Aerosol Optical Properties over Urban and Industrial Region of Northeast China
844 by Using Ground-based Sun-photometer Measurement. *Atmos. Environ.* 75: 270-278.
- 845 Zhao, H.J., Che, H.Z., Ma, Y.J., Xia, X.A., Wang, Y.F., Wang, P. and Wu, X.C. (2015). Temporal
846 Variability of the Visibility, Particulate Matter Mass Concentration and Aerosol Optical
847 Properties over an Urban Site in Northeast China. *Atmos. Res.* 166: 204-212.
- 848 Zheng, C.W., Zhao, C.F., Zhu, Y.N., Wang, Y., Shi, X.Q., Wu, X.L., Chen, T.M., Wu, F. and Qiu,
849 Y.M. (2017). Analysis of Influential Factors for the Relationship between PM_{2.5} and Aod in
850 Beijing. *Atmos. Chem. Phys.* 17: 13473-13489.
- 851 Zheng, Y., Che, H.Z., Yang, L.K., Chen, J., Wang, Y.Q., Xia, X.A., Zhao, H.J., Wang, H., Wang,
852 D.Y., Gui, K., An, L.C., Sun, T.Z., Yu, J., Kuang, X., Li, X., Sun, E.W., Zhao, D.P., Yang, D.S.,
853 Guo, Z.Y., Zhao, T.L. and Zhang, X.Y. (2017). Optical and Radiative Properties of Aerosols
854 during a Severe Haze Episode over the North China Plain in December 2016. *J. Meteor. Res.*
855 31: 1045-1061.
- 856 Zhu, J., Che, H.Z., Xia, X.A., Chen, H.B., Goloub, P. and Zhang, W.X. (2014).
857 Column-integrated Aerosol Optical and Physical Properties at a Regional Background
858 Atmosphere in North China Plain. *Atmos. Environ.* 84: 54-64.
- 859

860

Table Captions

861 **Table 1.** Monthly mean effective radii of aerosols and statistics of level 1.5 sun direct data for

862 AOD and Ångström exponent at Jiaozuo-HPU.

863 **Table 2.** Threshold values of aerosol properties for different absorbing types of aerosol.

864

865
866**Table 1.** Monthly mean effective radii of aerosols and statistics of level 1.5 sun direct data for AOD and Ångström exponent at Jiaozuo-HPU.

Month	R_{eff_t} (μm) ^a	$R_{\text{eff}_{\text{fine}}}$ (μm) ^b	$R_{\text{eff}_{\text{coarse}}}$ (μm) ^c	Days	Instantaneous Data
Jan	0.39 ± 0.13	0.15 ± 0.03	1.99 ± 0.36	15	553
Feb	0.41 ± 0.18	0.14 ± 0.06	2.06 ± 0.38	22	987
Mar	0.35 ± 0.08	0.15 ± 0.03	2.26 ± 0.36	14	462
Apr	0.44 ± 0.15	0.14 ± 0.05	2.07 ± 0.61	18	673
May	0.45 ± 0.13	0.14 ± 0.02	1.94 ± 0.56	24	924
Jun	0.30 ± 0.04	0.19 ± 0.03	2.43 ± 0.29	19	633
Jul	0.32 ± 0.06	0.22 ± 0.06	2.20 ± 0.42	36	1002
Aug	0.32 ± 0.07	0.22 ± 0.06	2.15 ± 0.27	28	820
Sep	0.35 ± 0.11	0.17 ± 0.04	2.40 ± 0.26	18	758
Oct	0.32 ± 0.04	0.21 ± 0.07	1.93 ± 0.39	12	361
Nov	0.34 ± 0.09	0.16 ± 0.04	1.93 ± 0.34	39	1394
Dec	0.33 ± 0.11	0.15 ± 0.04	2.13 ± 0.36	44	1571

867 ^a Effective radii of the total particles. ^b Effective radii of fine particles. ^c Effective radii of coarse particles.
868

869

Table 2. Threshold values of aerosol properties for different absorbing types of aerosol.

Group	Aerosol type	AE	SSA
Type I	Fine highly-absorbing	> 1.2	≤ 0.85
Type II	Fine moderately-absorbing	> 1.2	≥ 0.85 and < 0.9
Type III	Fine slightly absorbing	> 1.2	≥ 0.9 and < 0.95
Type IV	Fine non-absorbing	> 1.2	> 0.95
Type V	Mixed absorbing	≥ 0.6 and < 1.2	≤ 0.95
Type VI	Mixed non-absorbing	≥ 0.6 and < 1.2	> 0.95
Type VII	Coarse absorbing	≤ 1.2	≤ 0.95
Type VIII	Coarse non-absorbing	≤ 1.2	> 0.95

870

871

Figure Captions

873 **Fig. 1.** True color image and locations of Henan Province in China. The red dot denotes the
874 location of Jiaozuo-HPU.

Fig. 2. Monthly variation of (a) aerosol size distribution and (b) aerosol volumes at Jiaozuo-HPU.

Fig. 3. Monthly variations of (a) AOD_{440 nm}, (b) AE_{440-870 nm} and (c) water vapor content (WVC) at Jiaozuo-HPU. The boxes represent the 25th to 75th percentiles of the distributions while the middle line and red dots indicate the means and medians, respectively.

879 **Fig. 4.** Monthly variations of single scatter albedo (SSA) at 440, 670, 870 and 1020 nm at
 880 Jiaozuo-HPU.

Fig. 5. Monthly variations of (a) AAOD_{440 nm} and (b) AAE_{440-870 nm} at Jiaozuo-HPU. See Fig. 3 for an explanation of the symbols.

Fig. 6. The aerosol type classification using SSA, AE and FMF data for (a) annual, (b) spring, (c) summer, (d) autumn and (e) winter. See text in Table 2 for description of groups I-VIII.

Fig. 7. The frequency distribution of aerosol types for (a) annual, (b) spring, (c), summer, (d) autumn and (e) winter. See text in Table 2 for description of groups I-VIII.

887 **Fig. 8.** The correlation between AOD_{440 nm} and (a) relative humidity and (b) wind speed at
 888 Jiaozuo-HPU.

Fig. 9. MODIS Terra true color images during haze (a-g) and dust (h-k) events.

Fig. 10. The 72-h backward trajectories and the results of WPSCF and WCWT analysis during haze (a, b, c) and dust (d, e, f) events.

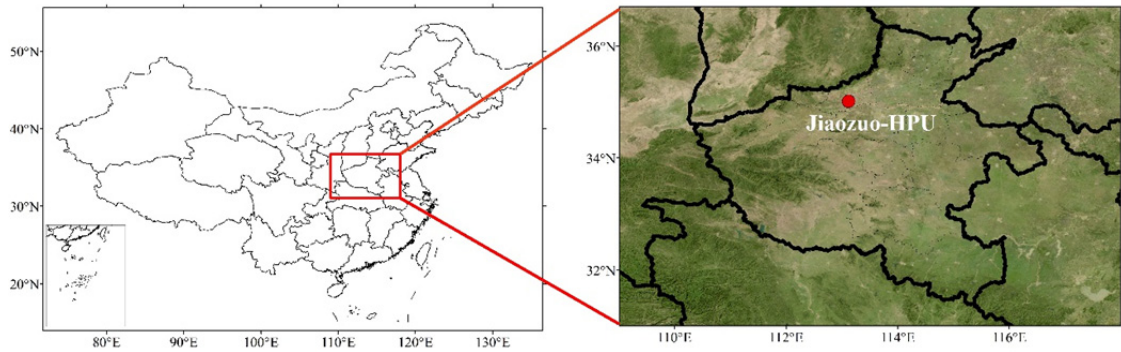
Fig. 11. CALIPSO total attenuated backscatter at 532 nm (top), volume depolarization ratio (middle), and aerosol subtype (bottom) on the daytime of May 3 and 5 and the nighttime of May

894 4 and 6.

895 **Fig. 12.** Daily average wind fields at (a) the surface during haze and (b) 750hPa during dust in
896 Henan Province areas. The red dot denotes the Jiaozuo-HPU site.

897 **Fig. 13.** Daily average values of (a, b) AOD, AE, PM concentration, (c, d) volume size
898 distribution, (e, f) AAOD and (g, h) SSA at Jiaozuo-HPU for haze and dust events, respectively.

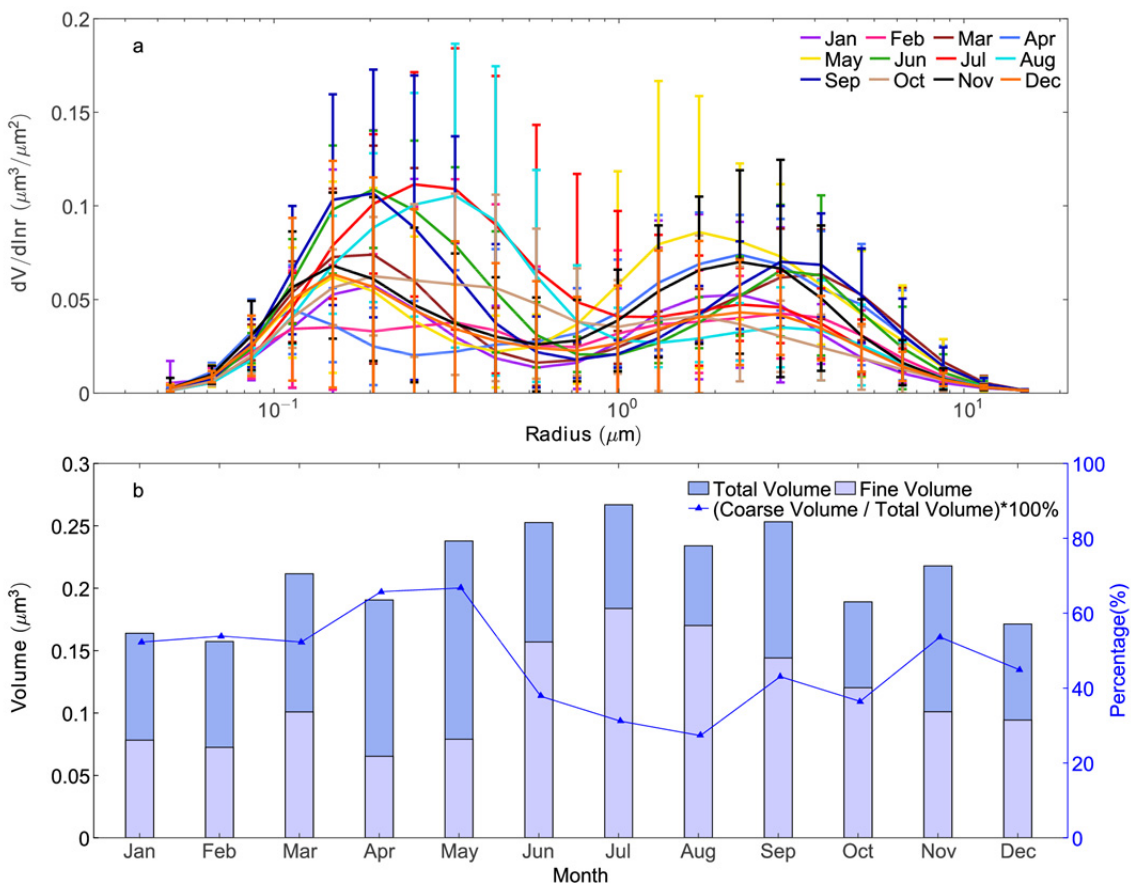
899



900

901 **Fig. 1.** True color image and locations of Henan Province in China. The red dot denotes the
902 location of Jiaozuo-HPU.

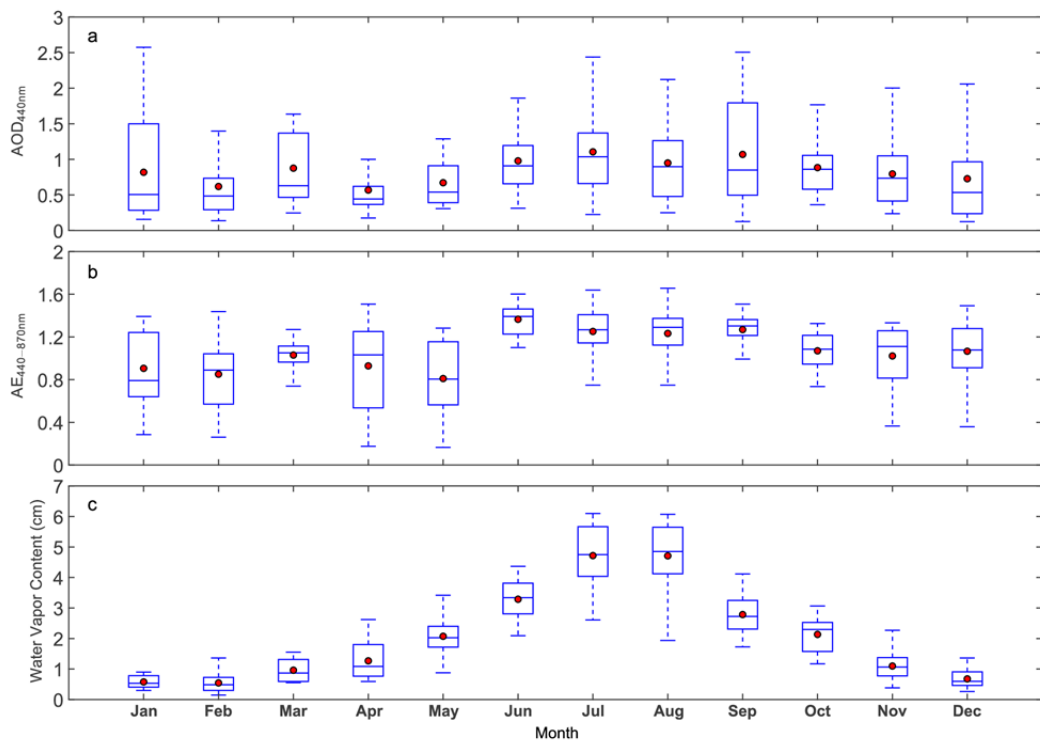
903



904

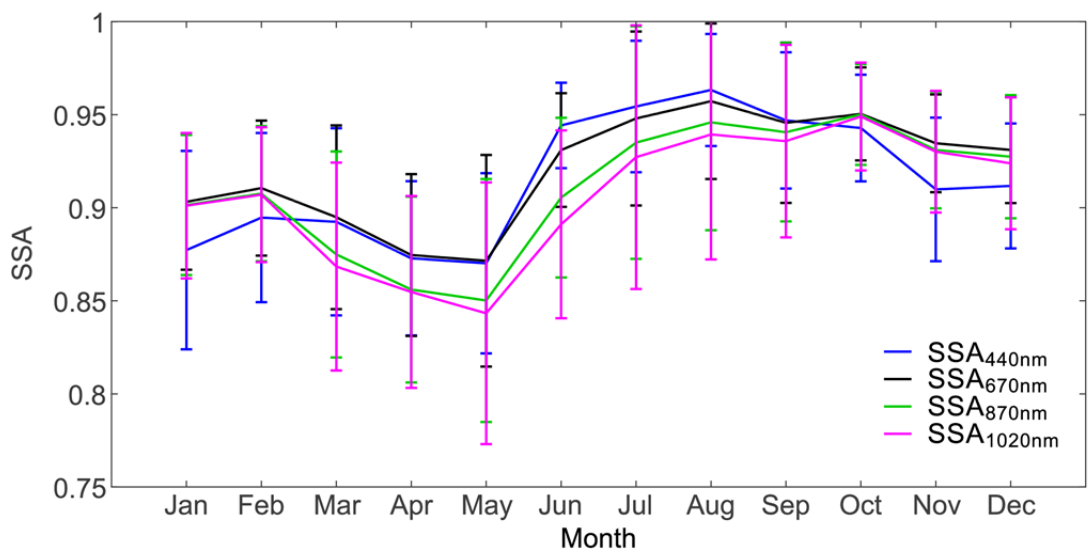
905 **Fig. 2.** Monthly variation of (a) aerosol size distribution and (b) aerosol volumes at Jiaozuo-HPU.

906



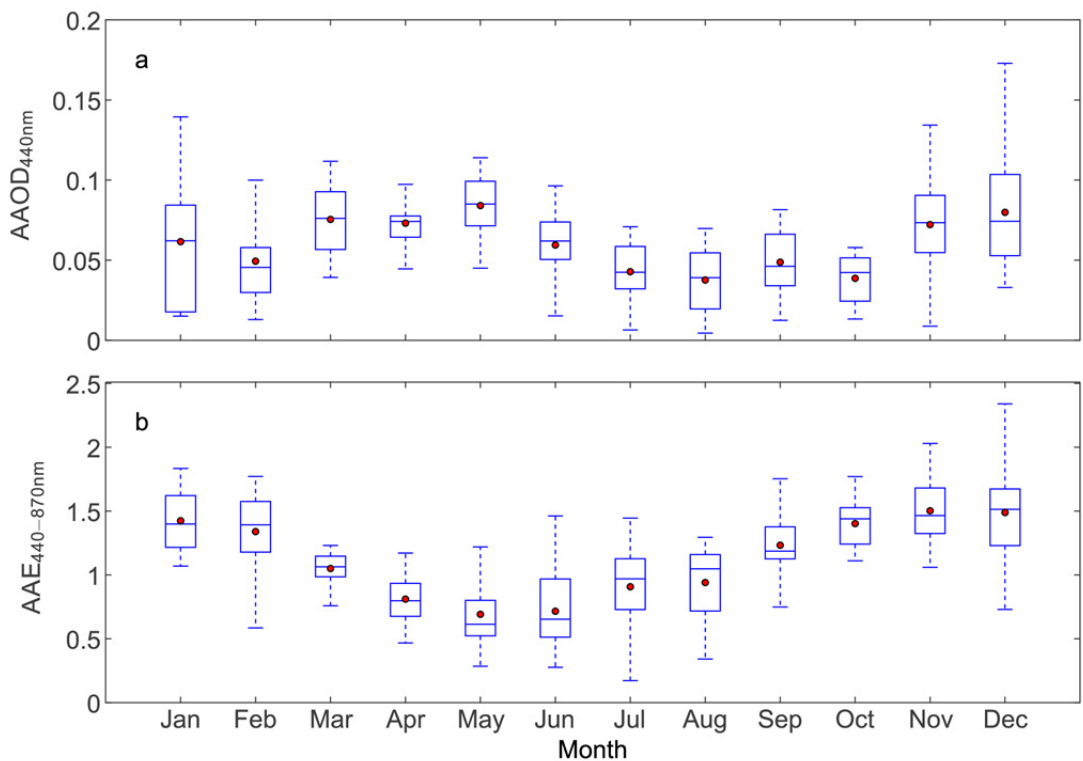
907

908 **Fig. 3.** Monthly variations of (a) AOD_{440 nm}, (b) AE_{440-870 nm} and (c) water vapor content (WVC)
 909 at Jiaozuo-HPU. The boxes represent the 25th to 75th percentiles of the distributions while the
 910 middle line and red dots indicate the means and medians, respectively.
 911



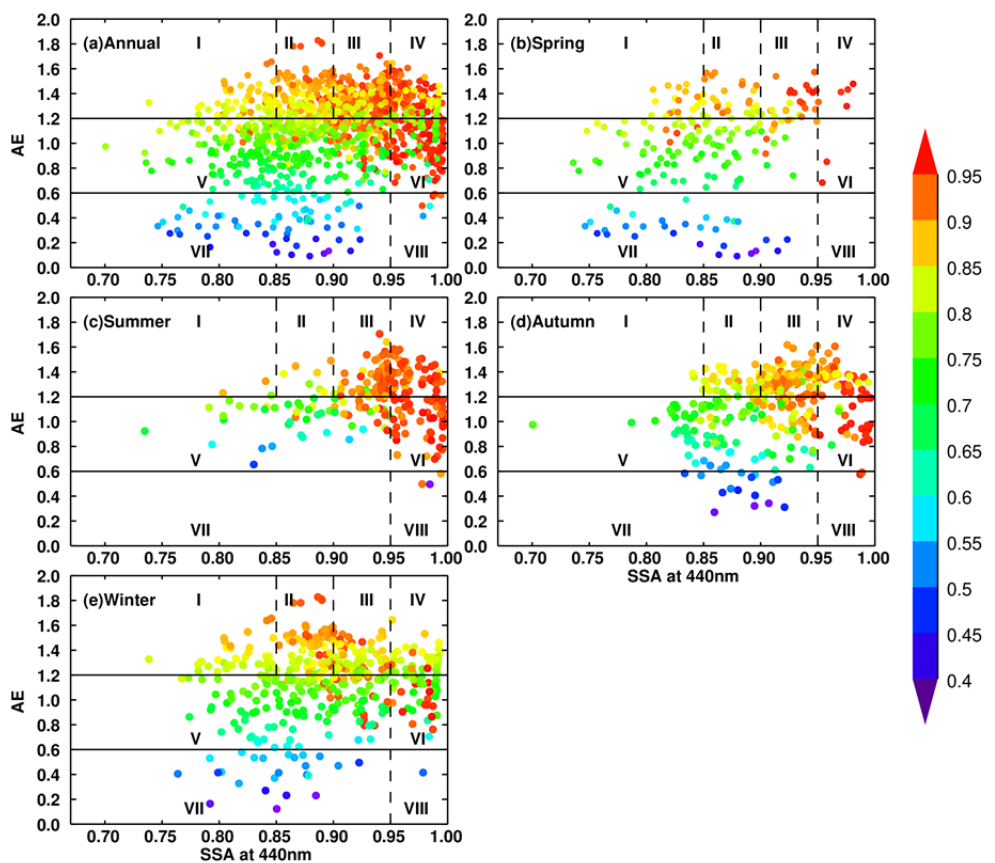
912

913 **Fig. 4.** Monthly variations of single scatter albedo (SSA) at 440, 670, 870 and 1020 nm at
 914 Jiaozuo-HPU.
 915



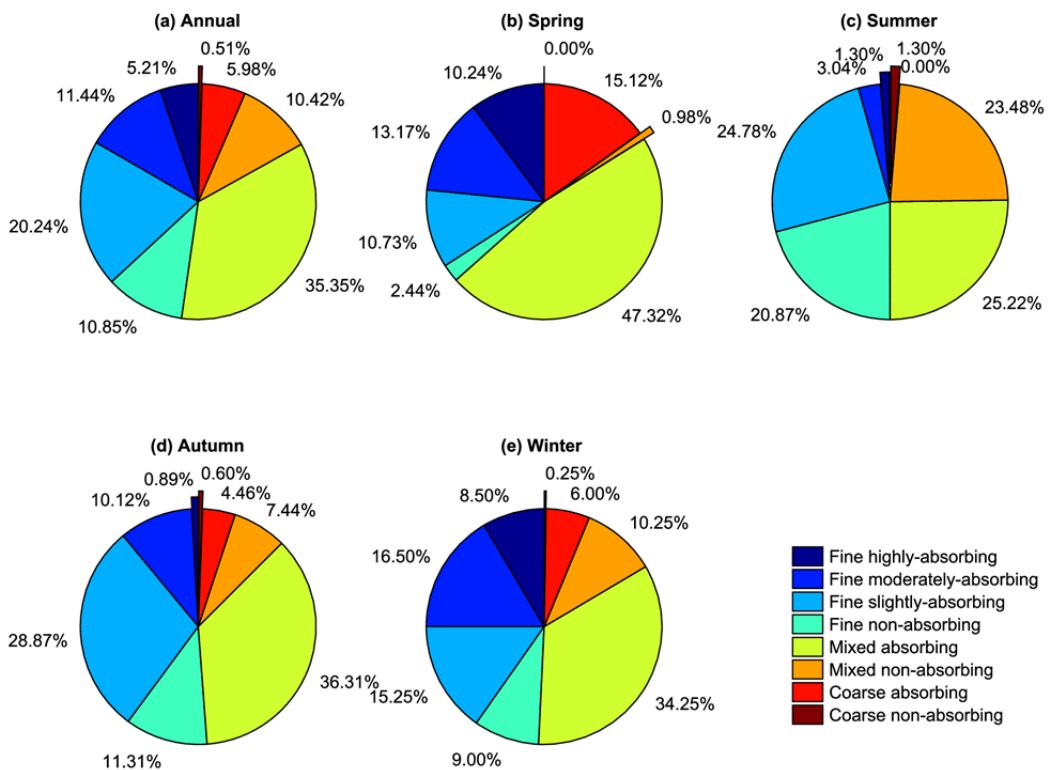
916

917 **Fig. 5.** Monthly variations of (a) AAOD_{440 nm} and (b) AAE_{440-870 nm} at Jiaozuo-HPU. See Fig. 3
918 for an explanation of the symbols.
919



920

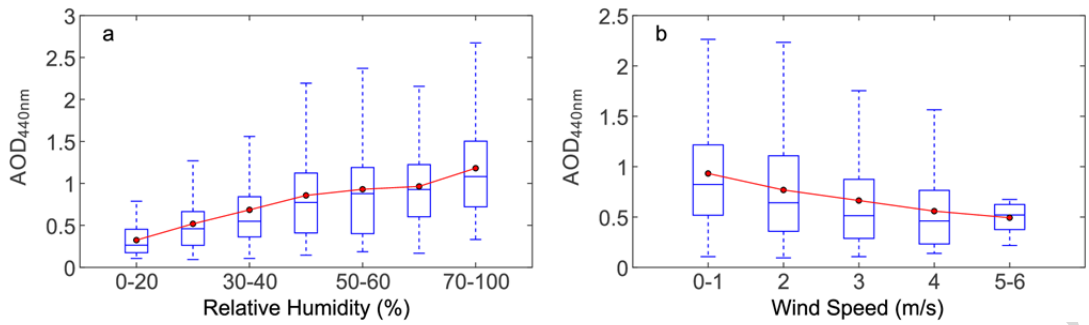
921 **Fig. 6.** The aerosol type classification using SSA, AE and FMF data for (a) annual, (b) spring, (c),
 922 summer, (d) autumn and (e) winter. See text in Table 2 for description of groups I-VIII.
 923



924

925 **Fig. 7.** The frequency distribution of aerosol types for (a) annual, (b) spring, (c), summer, (d)
 926 autumn and (e) winter. See text in Table 2 for description of groups I-VIII.

927

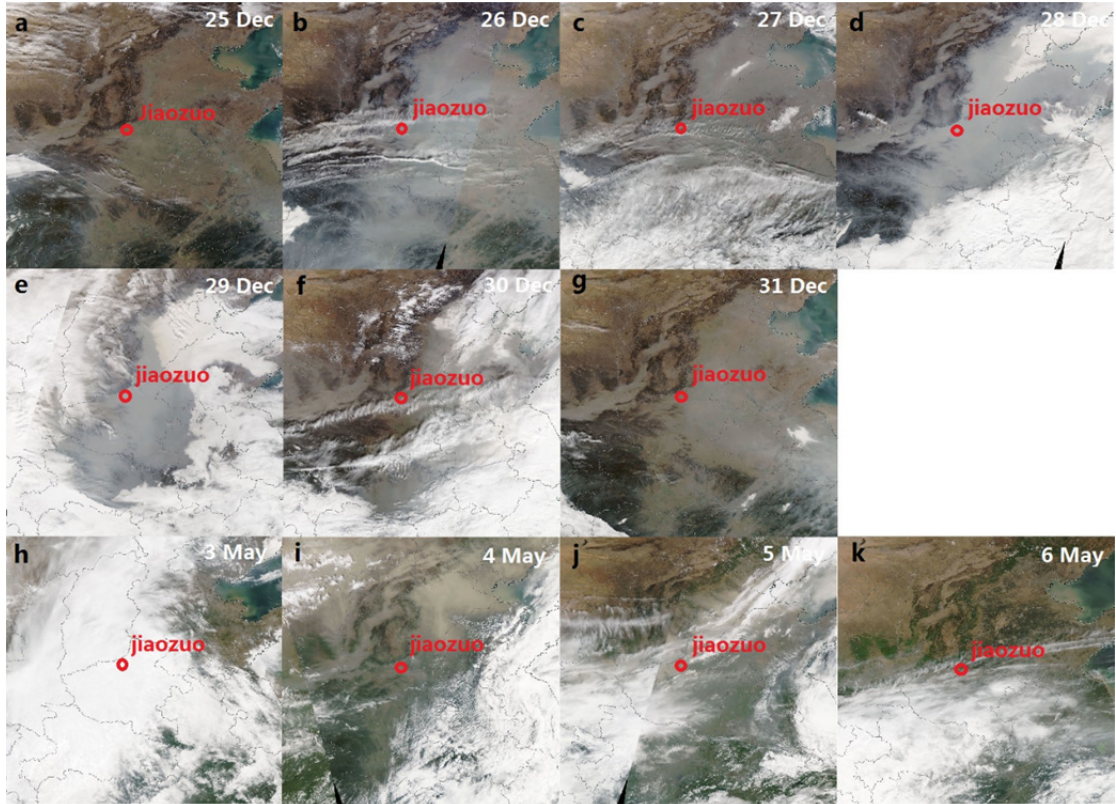


928

929 **Fig. 8.** The correlation between AOD_{440 nm} and (a) relative humidity and (b) wind speed at

930 Jiaozuo-HPU.

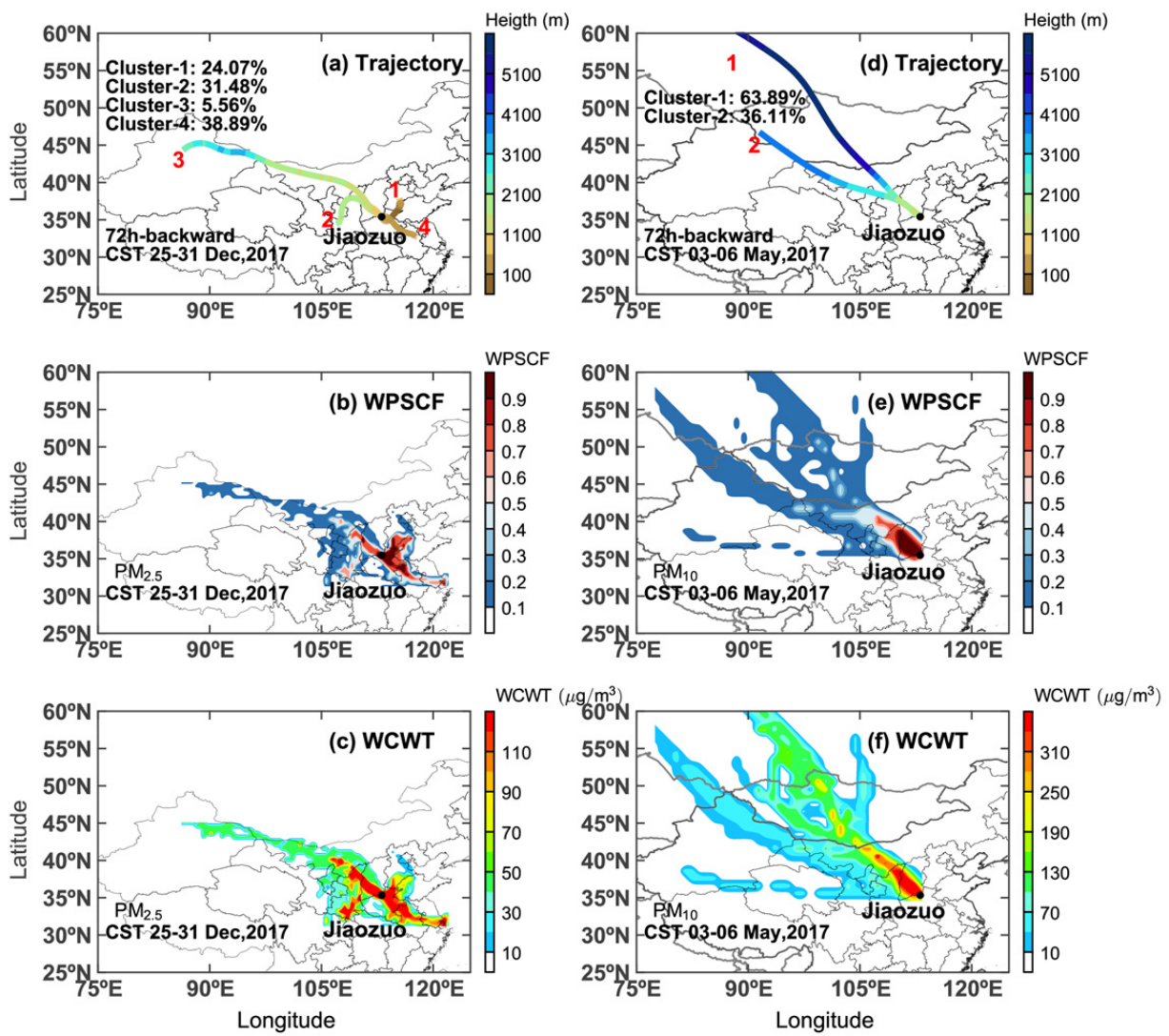
931



932

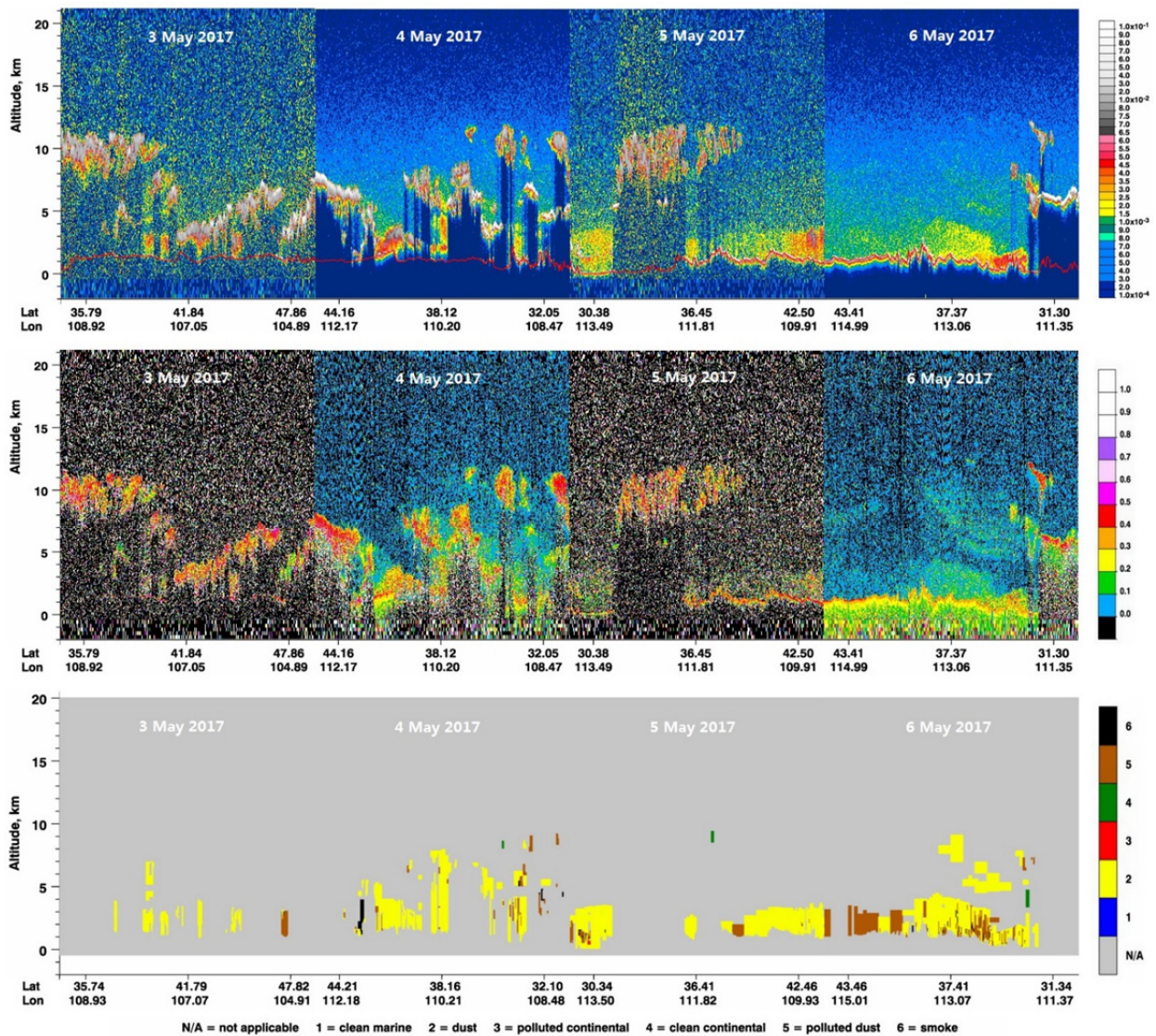
933

Fig. 9. MODIS Terra true color images during haze (a-g) and dust (h-k) events.



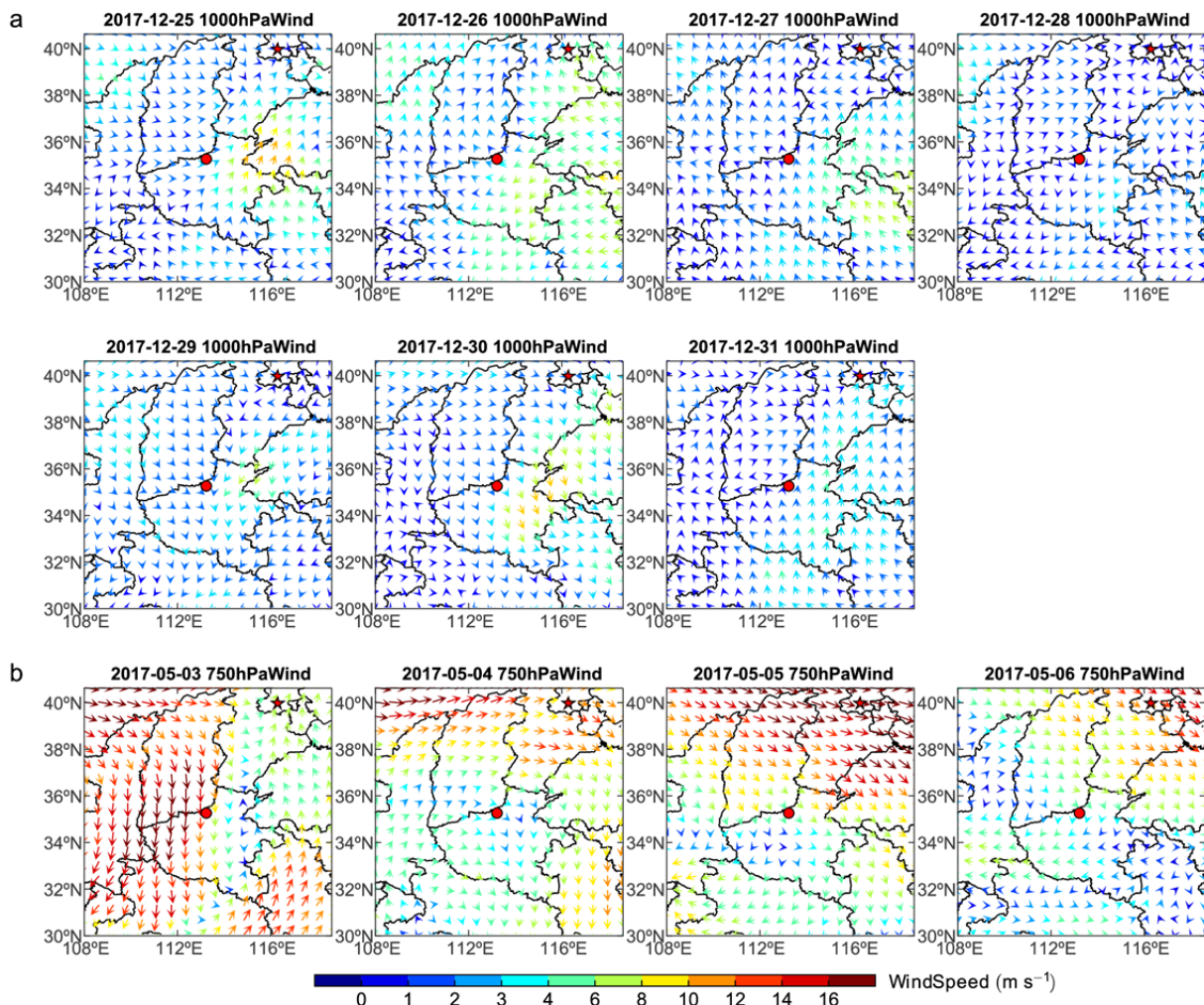
934

935 **Fig. 10.** The 72-h backward trajectories and the results of WPSCF and WCWT analysis during
 936 haze (a, b, c) and dust (d, e, f) events.



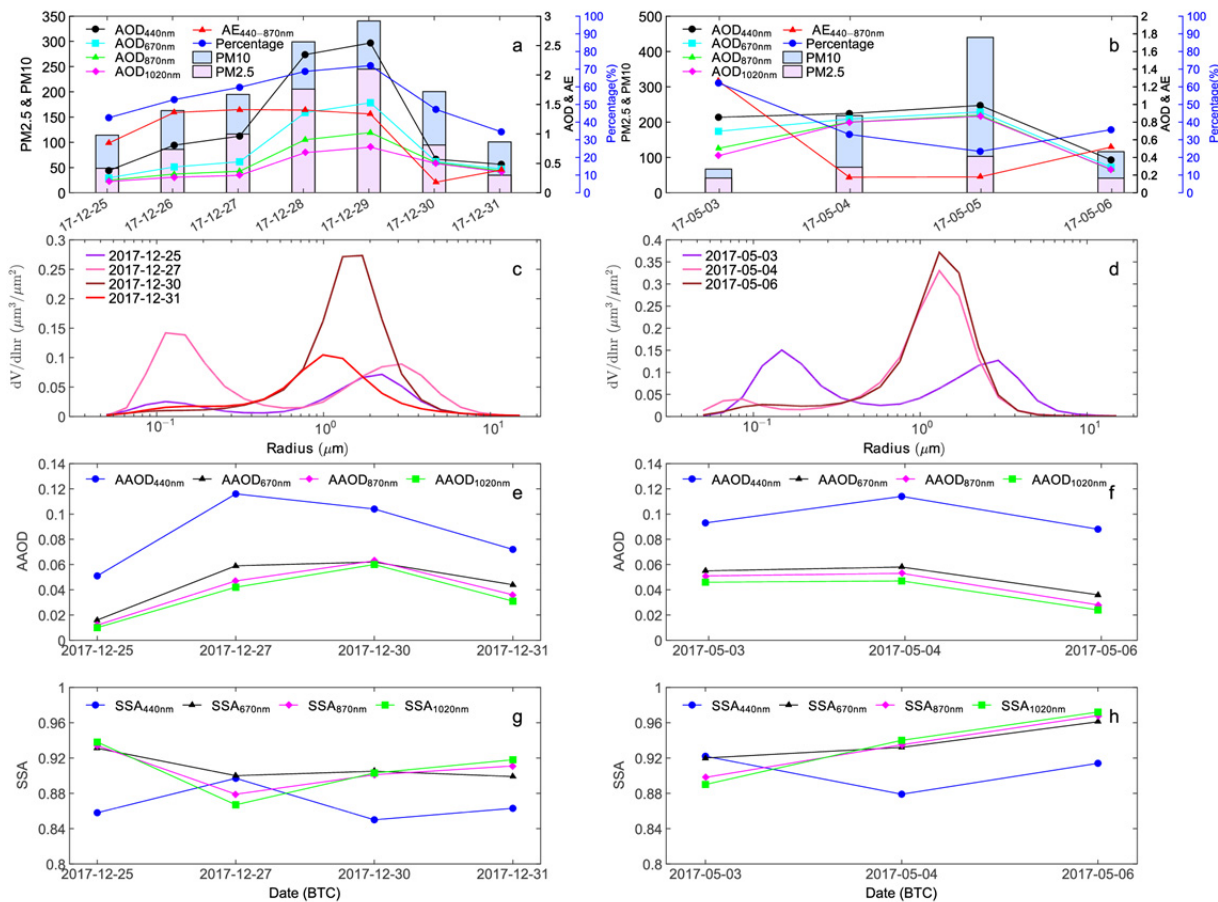
937

938 **Fig. 11.** CALIPSO total attenuated backscatter at 532 nm (top), volume depolarization ratio
 939 (middle), and aerosol subtype (bottom) on the daytime of May 3 and 5 and the nighttime of May
 940 4 and 6.



941

942 **Fig. 12.** Daily average wind fields at (a) the surface during haze and (b) 750hPa during dust in
 943 Henan Province areas. The red dot denotes the Jiaozuo-HPU site.



944

945 **Fig. 13.** Daily average values of (a, b) AOD, AE, PM concentration, (c, d) volume size
946 distribution, (e, f) AAOD and (g, h) SSA at Jiaozuo-HPU for haze and dust events, respectively.